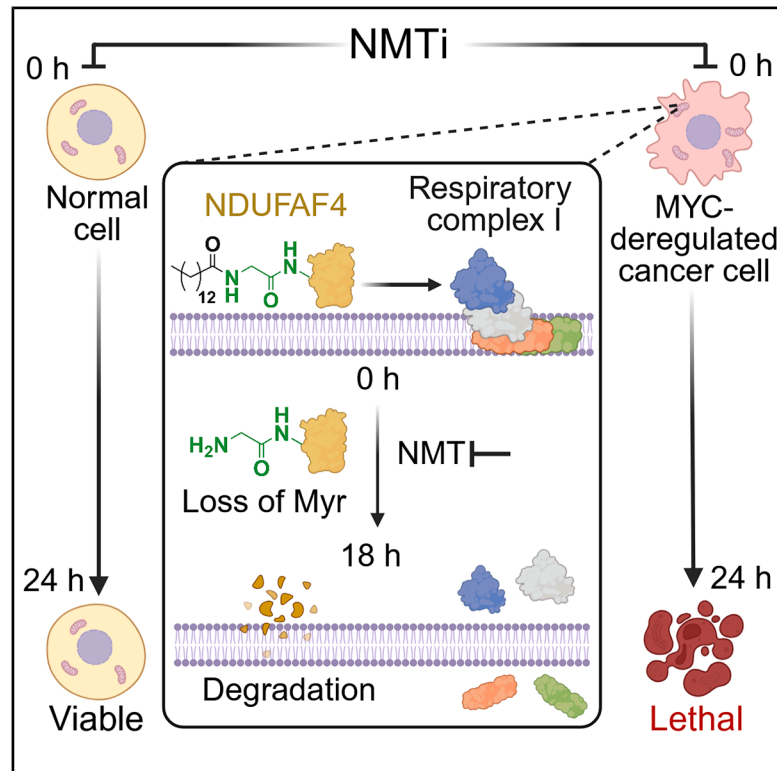# MYC deregulation sensitizes cancer cells to *N*-myristoyltransferase inhibition

Graphical abstract

Authors

Gregor A. Lueg, James Zhang, Monica Faronato, ..., Louis Chesler, Dinis P. Calado, Edward W. Tate

Correspondence

dinis.calado@crick.ac.uk (D.P.C.),
e.tate@imperial.ac.uk (E.W.T.)

In brief

Lueg et al. discovered that deregulated MYC increases cancer cell sensitivity to *N*-myristoyltransferase inhibitors (NMTis). Mitochondrial dysfunction upon NMTi occurs selectively in high-MYC contexts through impaired complex I via effects on the NMT substrate and complex I assembly factor NDUFAF4. An approach for targeting MYC-driven cancers is revealed.

Highlights

- Deregulated MYC sensitizes cancer cells to NMT inhibitors

- Complex I proteins are depleted upon NMT inhibition in MYC deregulated cells

- Loss of NDUFAF4 *N*-myristoylation is linked to mitochondrial dysfunction

- NMT inhibitors are efficacious and tolerated in mouse models of MYC-driven cancer

CellPress

CellPress
OPEN ACCESS

Article

MYC deregulation sensitizes cancer cells to *N*-myristoyltransferase inhibition

Gregor A. Lueg,[1,2,8] James Zhang,[1,2,3,8] Monica Faronato,[1,2,8] Andrii Gorelik,[1,2,8] Wouter W. Kallemeijn,[1,2] Francesco Falciani,[4] Josephine Walton,[1,4] Jack W. Houghton,[1] Silvia Vannini,[1] Evon Poon,[3] Barbara M. Costa,[3] Roberto Solari,[4] Robin Carr,[4] Andrew S. Bell,[1,4] Edward J. Bartlett,[1] Bernadette Brzezicha,[5] Martin Janz,[6] Louis Chesler,[3] Dinis P. Calado,[2,7,*] and Edward W. Tate[1,2,4,9,*]

[1]Department of Chemistry, Molecular Sciences Research Hub, White City Campus, Imperial College London, 82 Wood Lane, W12 0BZ London, UK
[2]The Francis Crick Institute, 1 Midland Road, NW1 1AT London, UK
[3]Division of Clinical Studies, The Institute of Cancer Research (ICR) & Royal Marsden NHS Trust, SW3 6JB London, UK
[4]Myricx Pharma Limited, London Innovation Centre, 20 Water Street, E14 5GX London, UK
[5]Experimental Pharmacology & Oncology Berlin-Buch, Robert-Rössle-Str. 10, 13125 Berlin, Germany
[6]Experimental and Clinical Research Center, Max Delbrück Center for Molecular Medicine and Charité – Universitätsmedizin Berlin, 13125 Berlin, Germany
[7]Peter Gorer Department of Immunobiology, School of Immunology & Microbial Sciences, King's College London, The Francis Crick, SE1 9RT London, UK
[8]These authors contributed equally
[9]Lead contact
*Correspondence: dinis.calado@crick.ac.uk (D.P.C.), e.tate@imperial.ac.uk (E.W.T.)
https://doi.org/10.1016/j.celrep.2025.116180

SUMMARY

Human *N*-myristoyltransferases (NMTs) catalyze N-terminal protein *N*-myristoylation and are promising targets in cancer, with an emerging mechanistic rationale for targeted therapy. Here, we screened 245 cancer cell lines against IMP-1320, a potent NMT inhibitor (NMTi), and conducted pathway-level analyses to identify that deregulated MYC increases cancer cell sensitivity to NMTis. Proteomics on detergent-enriched membrane fractions in MYC or MYCN-deregulated cancer cell models revealed that cell death is associated at least in part with loss of membrane association of mitochondrial respiratory complex I. This is concurrent with loss of myristoylation and degradation of the complex I assembly factor NDUFAF4, and induction of mitochondrial dysfunction, driven by MYC or MYCN-deregulation. NMTis eliminated or suppressed MYC- and MYCN-driven tumors *in vivo* without overt toxicity, suggesting that this constitutive co-translational protein modification can be targeted in MYC-driven cancers.

INTRODUCTION

N-Myristoylation is an irreversible lipid modification of proteins at an N-terminal glycine, mediated in humans by two closely related *N*-myristoyltransferases, NMT1 and NMT2 (Figure 1A).[1] The substrate and acyl-CoA-binding sites of NMT1 and NMT2 are highly conserved, whereas the two isozymes differ predominantly in their N-termini, which is dispensable for catalysis but may be involved in cellular localization.[2] However, current evidence suggests that cellular *N*-myristoylation is predominantly catalyzed by NMT1, at least in developing T cells and embryonic stem cells.[3,4] *N*-Myristoylation modulates membrane association,[5,6] protein stability,[7] and protein-protein interactions,[8] and proteomic and bioinformatic studies have identified over 200 substrates of NMT in the human proteome.[9–11] Most substrates are modified co-translationally at the ribosome after processing by methionine aminopeptidases (MetAPs), although post-translational *N*-myristoylation on neo-N-termini exposed after protease cleavage has been observed.[9] A wide range of cellular pathways are modulated by NMT substrates, including mTORC1 signaling,[12,13] proteasomal degradation,[14] and protein trafficking,[15,16] supporting the central importance of this modification to cellular homeostasis. It is therefore unsurprising that multiple *N*-myristoylated proteins have been associated with pro-oncogenic activity,[17] including well-known oncoproteins such as SRC, ABL2, and PRKACA.[18] As a result, targeting cancer through the global ablation of *N*-myristoylation by NMT inhibition has been proposed,[19] although a mechanistic rationale supporting a sufficient therapeutic index for NMT inhibition has been lacking. Many prior studies were limited by a lack of potent NMT inhibitors (NMTis; Figures 1B and S1A),[20] which have only recently been reported.[21] Furthermore, past studies have predominantly focused on selected individual NMT substrates[22] rather than addressing the broad consequences of NMT inhibition, despite the pleiotropic effect of NMTi on diverse cellular pathways.[19,23]

MYC proteins (MYC, MYCN, and MYCL) are a family of transcription factors that are highly implicated in tumorigenesis
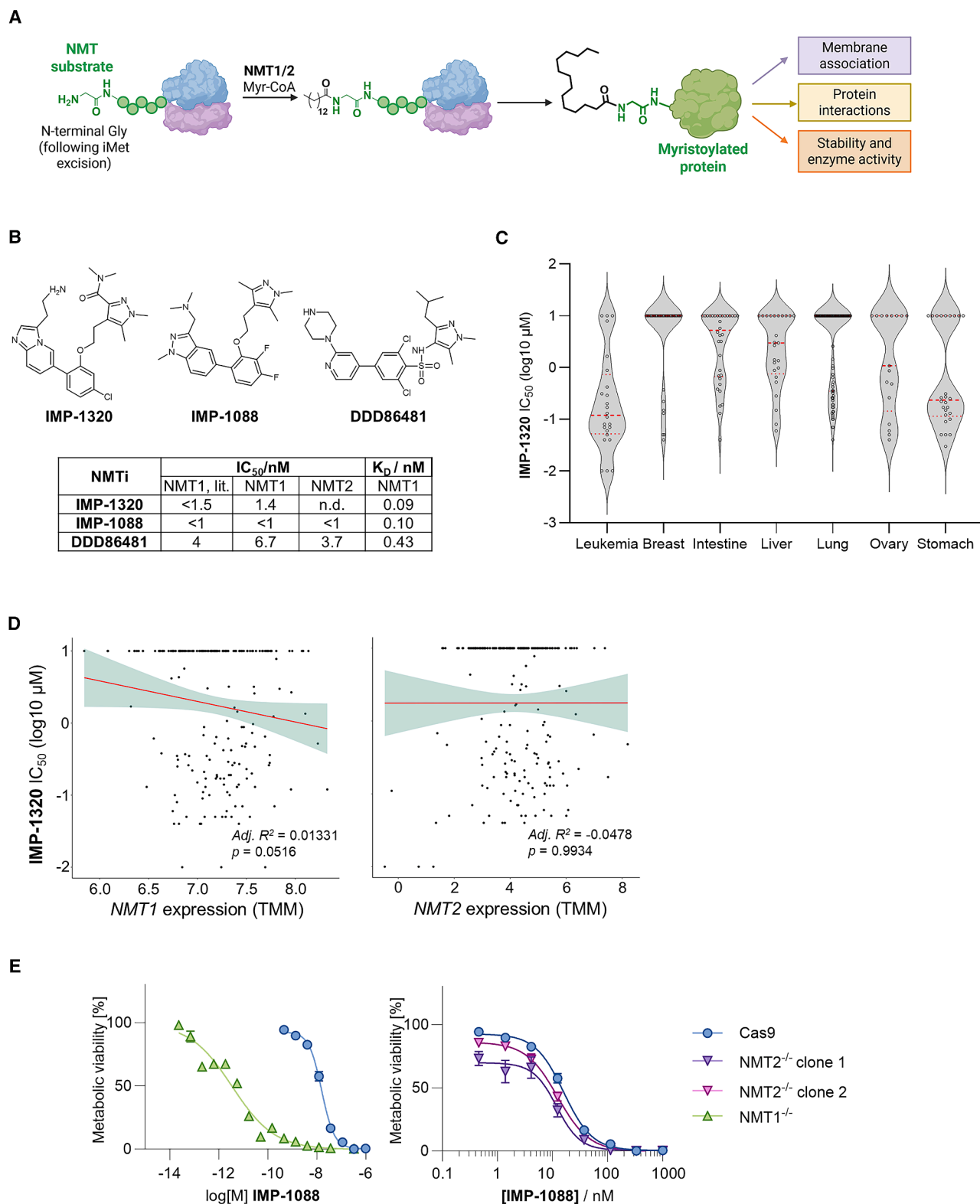
Figure 1. Cancer subtype, but not NMT1 or NMT2 expression, predicts sensitivity to NMTis in a diverse cancer cell line screen

(A) Human NMT1 and NMT2 catalyze protein *N*-myristoylation of specific substrates during peptide elongation at the ribosome, leading to varied functions for the NMT substrate.

(legend continued on next page)

and tumor maintenance.[26] The MYC transcriptional program promotes protein synthesis, metabolic remodeling, and ribosomal and mitochondrial biogenesis, ultimately contributing to many of the hallmarks of cancer.[27] Deregulation of MYC proteins is present in the majority of cancers, although the paralogs deregulated differ between types of cancer. While MYC is altered ubiquitously, MYCN deregulation is enriched in tumors of neuronal and neuroendocrine origin, and MYCL deregulation is most commonly associated with small-cell lung cancer.[28] Importantly, deregulation of MYC proteins is often associated with aggressive disease and poor prognosis, but MYC proteins currently remain intractable drug targets due to their unstructured nature.[29,30]

Here, we combined large-scale cancer cell line screening against a potent and specific NMTi with pathway-level analysis of cell state, revealing that deregulation of MYC renders cancer cells acutely sensitive to NMT inhibition. Analyses of detergent-enriched membrane fractions in separate models of MYC- and MYCN-deregulated cells showed that NMTi-induced cell death in these contexts is associated with loss of mitochondrial respiratory complex I proteins. This is concurrent with depletion of the N-myristoylated complex I assembly factor NDUFAF4 and induction of mitochondrial dysfunction selectively in MYC-deregulated contexts. NMTi inhibited or eliminated MYC- and MYCN-driven tumors *in vivo* without overt toxicity, providing a mechanistic framework for NMTi as a targeted cancer therapy. This work offers examples of targeting a constitutive co-translational protein modification in MYC-deregulated cancers and potentially presents an avenue to target cancers driven by this class of intractable oncoproteins.[29,30]

RESULTS

NMT expression does not correlate with NMTi sensitivity in a cell line screen

First, we set out to discover which cancer subtypes are highly sensitive to NMT inhibition. We screened a panel of 245 cancer cell lines, spanning a range of cancer types against a range of concentrations of IMP-1320 (Figures 1B and S1A),[15,24] a highly potent NMTi sharing a similar core structure as the previously reported and commonly used tool NMTi IMP-1088,[21] albeit with improved pharmacokinetic properties. IMP-1320 was effective in a subset of all cancer types tested, particularly in leukemia cancer cell lines (Figures 1C and S1B; Table S1),[22] and expression of *NMT1* or *NMT2* did not correlate with IC_{50} values across the cell line panel (Figure 1D), consistent with previous screens against DDD86481, an NMT inhibitor from a different chemical class.[22,23,25] Consistent with cellular N-myristoylation catalyzed predominantly by NMT1,[3] whole-genome CRISPR KO screens

(Cancer Dependency Map, DepMap[31,32]) processed with a common pipeline[33] identified NMT1 as required for optimal proliferation (common essential) of most cancer cell lines, whereas NMT2 lacked essentiality in any cell line tested (Figure S1C). The gene effect score of *NMT1* KO is also significantly correlated with *NMT2* expression,[23] likely due to partial rescue of N-myristoylation by NMT2. However, CRISPR-Cas9 NMT1 homozygous knockout in HeLa cells (Figures S1D and S1E) conferred 1,000-fold greater sensitivity to IMP-1088,[21] shifting the EC_{50} value from 10 nM to 10 pM, whereas NMT2 knockout had minimal impact (Figure 1E), consistent with a negligible impact of NMT2 expression on NMTi sensitivity. Notably, all potent human NMTis reported to date are dual NMT1 and NMT2 inhibitors, due to the very high homology of these isoforms in the catalytic domain.[11,34] It is therefore likely that genetic associations with differential NMT expression do not apply in the context of pharmacological inhibition of NMTs due to concurrent inhibition of both enzymes.

MYC deregulation sensitizes cancer cells to NMTi

To identify biologically relevant predictors for NMTi sensitivity, we used single sample gene set enrichment analysis (ssGSEA)[35] to obtain enrichment scores for the Hallmark gene sets[36] in 211 cell lines with publicly available transcriptomic annotation[37] (Figure 2A). Cell lines were classified as sensitive ($IC_{50} < 0.2\ \mu M$) or less sensitive ($IC_{50} > 0.2\ \mu M$) to IMP-1320. Using a linear model, we then identified gene sets with significantly altered enrichment scores (FDR <1%) between sensitive and less sensitive cell lines and found 11 gene sets that correlated with sensitivity to NMT inhibition, with the majority being less expressed in sensitive cell lines (Figure 2B). These results were broadly consistent across a range of sensitivity thresholds and also with a no-threshold method to identify significant gene sets, confirming their validity. Treating each gene set as a binary operator, the area under the curve (AUC) of the receiver operating curve (ROC) confirmed that these gene sets individually predicted sensitivity to NMT inhibition (Figure S2A). Notably, transcription of MYC target V1 was both significantly enriched in sensitive lines and predictive of sensitivity (Figure 2C), a finding consistent with previously reported screens using DDD86481.[23] Furthermore, cancer cell lines with greater dependence on NMT1 expression were also overrepresented in high MYC expression and/or structural alterations in MYC or MYCN (Figure S2B).

We next explored the hypothesis that deregulated MYC increases sensitivity of cancer cells to NMTi using IMP-1088, a thoroughly validated, highly potent, and widely used NMTi in P493-6 immortalized B cells. These cells are a model of Burkitt's lymphoma,[38] a cancer type that has previously been shown to be


(B) Chemical structure, NMT1 binding affinity, and inhibitory potency against human NMT1 and NMT2 for the NMTi used in this study. IC_{50} values from literature (lit.) are taken from refs. [21,24] and [25]. IC_{50} values were experimentally determined in this study by the CPM assay, in which IC_{50}s below 5 nM cannot be accurately determined.

(C) Violin plots of the distribution of IMP-1320 IC_{50} values across the cell line panel by tissue of origin. The values for undetermined IC_{50} values were set to 1.

(D) Correlation between IMP-1320 IC_{50} values and *NMT1* (left) and *NMT2* (right) expression in the cell line panel. Spearman correlation coefficients are shown.

(E) Sensitization to NMT inhibition by IMP-1088 in HeLa NMT1$^{-/-}$ and NMT2$^{-/-}$ cells (CellTiter-Blue assay). Left, responses for the NMT1$^{-/-}$ line generated. Right, responses for the NMT2$^{-/-}$ lines generated. Data are shown as mean ± SEM of at least n = 3 biological replicates. Figure 1A was created in BioRender. Zhang, J. (2025) https://BioRender.com/y5dssjj. See also Figure S1.

A

B

C

D

E

F

G
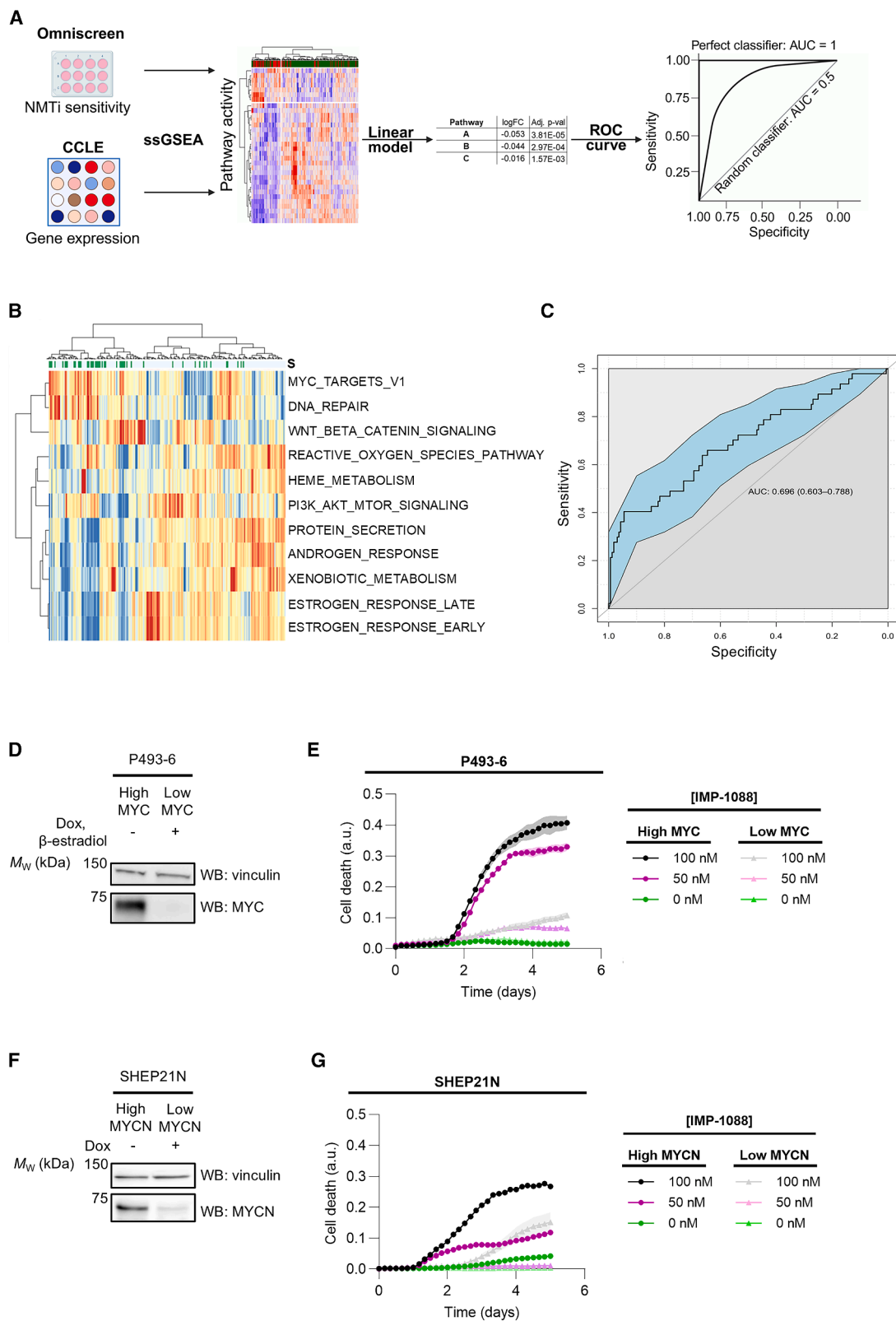
(legend on next page)

highly sensitive to NMT inhibition.[22] Importantly, they highly express MYC, which can be suppressed by a combination of doxycycline and β-estradiol, allowing investigation of MYC-mediated effects. MYC was regulated to high or low levels over 24 h[38] (Figure 2D), and cells subsequently exposed to various concentrations of IMP-1088 for 5 days with cell death determined by SYTOX Green staining as a readout for NMTi sensitivity. Cell death was highly pronounced in high-MYC P493-6 cells upon treatment with 100 nM IMP-1088, a concentration sufficient to robustly inhibit cellular NMT activity as observed by metabolic labeling with myristate analogue YnMyr[20,39] (Figure S2C), whereas minimal death occurred in low-MYC P493-6 cells (Figure 2E). Similar sensitivity was observed in MYCN *tet*-off SHEP21N cells,[40] a model of a highly aggressive form of clinical neuroblastoma (NB) driven primarily by *MYCN*-amplification[41] (Figure 2F). High-MYCN SHEP21N cells treated with NMTi experienced high levels of cytotoxicity relative to DMSO-treated controls, whereas low-MYCN SHEP21N cells were less sensitive, again at concentrations that inhibit cellular *N*-myristoylation (Figures 2G and S2C). However, NMTi did not deplete MYC or MYCN levels in either model, consistent with a sensitizing mechanism downstream of MYC/MYCN expression (Figure S2D). The dependency of NMTi efficacy on MYC or MYCN was confirmed by cell quantification assays (Figure S2E) in P493-6 cells and MYCN-ER-SHEP cells, a neuroblastoma cell line in which 4-hydroxytamoxifen (tam) induces MYCN,[42] and also using a chemically distinct and potent NMTi (DDD86481[43]), confirming the role of on-target NMT inhibition in cell death. Collectively, these data support MYC deregulation as a sensitizing factor for NMTi in cancer cells.

## NMTi drives mitochondrial dysfunction in high-MYC cancer cells

Many of the >200 known human *N*-myristoylated proteins associate dynamically with membranes,[1] and the myristoyl group frequently plays a critical role in mediating membrane localization.[44] We therefore hypothesized that a key downstream consequence of NMT inhibition would be mis-localization or depletion of biologically relevant protein complexes from the membrane and that the combined effect of multiple *N*-myristoylated proteins on these complexes and their interactors may be enough to significantly affect their function. We therefore isolated detergent-enriched membrane fractions (detergent fractions) through Triton X-114 (TX-114) phase separation[45] and applied LC-MS/MS-based analysis to determine changes upon NMTi treatment

(Figure 3A), which may result from changed protein abundance or localization. We first examined the effect in high-MYC P493-6 cells treated with 100 nM IMP-1088 for 24 h, just prior to the onset of significant cell death. Overall, 3,532 proteins were identified, of which 72% had UniProt membrane annotations and 87 are known to be co-translationally *N*-myristoylated.[11,19] As expected, the predominant effect of NMT inhibition was to deplete *N*-myristoylated proteins in detergent fractions (Figure S3A). All significantly affected NMT substrates ($p < 0.05$, 53 proteins) were depleted in this fraction by NMTi, with a majority of these highly affected (log2 fold change < −0.585). Protein-protein interaction analysis of all proteins significantly depleted in the detergent fraction by NMTi ($p < 0.05$, 273 proteins, Figure 3B) using the stringApp Cytoscape plugin[46] revealed several distinct protein clusters, including several pathways previously reported to be affected downstream of NMT inhibition, such as mTOR signaling through the Ragulator-Rag complex.[12,13] However, the cluster with the most affected proteins is related to mitochondrial respiratory complex I, consistent with previously reported impacts on complex I at the whole proteome level upon NMT inhibition[19,47] or NMT1 KO.[23] An analogous experiment in high-MYCN SHEP21N cells produced similar results in terms of affected biological functions (Figures 3C and S3B), implying a conserved mechanism of action across MYC paralogues.

MYC upregulation is known to drastically increase mitochondrial biogenesis,[48,49] and inhibitors of oxidative phosphorylation have demonstrated efficacy in MYC- or MYCN-expressing cancer cells including *MYCN*-amplified neuroblastoma[49,50] and B cell lymphomas.[51–53] We therefore hypothesized that disruption of complex I, provoked by NMTi, causes a failure in mitochondrial function in high-MYC cancer models,[54] contributing to cell death. We confirmed increased mitochondrial respiration in high-MYC P493-6 or high-MYCN SHEP21N cells compared to low-MYC P493-6 or low-MYCN SHEP21N cells (Figure 3D), as previously reported,[49,55,56] and found that exposure of high-MYC or high-MYCN cells to NMTi significantly ($p < 0.05$) reduced respiratory parameters, whereas low-MYC or low-MYCN cells were unaffected by NMTi treatment (Figures 3E, S3C, and S3D). These effects were already observable after only 12-h NMTi treatment in high-MYC P493-6 cells (Figure S3E). Additionally, in high-MYC, but not low-MYC, P493-6 cells, IMP-1088 treatment (100 nM, 18 h) decreased mitochondrial potential and increased superoxide generation (Figure S3F). Notably, both IMP-1088 and DDD86481 induced similar impacts on mitochondrial function in

Figure 2. MYC deregulation sensitizes cells to NMT inhibition

(A) Strategy to identify biological pathways enriched in NMTi-sensitive lines (IC$_{50}$ < 0.2 μM). ssGSEA was performed for 211 cell lines with publicly available expression data (DepMap) to characterize cell lines in terms of pathway expression. Using a linear model differentially expressed gene sets in sensitive vs. less sensitive cell lines were identified. The ability of these gene sets to predict sensitivity to NMTis was then assessed using an ROC curve.

(B) Heatmap showing the Hallmark gene sets predictive for NMTi sensitivity (FDR<0.01) and their expression in each cell line. Sensitive cell lines are marked by a green bar. Red indicates higher expression; blue indicates lower expression.

(C) ROC curve for MYC target V1 as a predictor for NMTi sensitivity.

(D) Western blot for MYC in P493-6 cells with or without doxycycline and β-estradiol treatment.

(E) Real-time cytotoxicity assay for IMP-1088 in high and low-MYC P493-6 cells. A representative biological replicate is shown as mean ± SEM of *n* = 3 technical replicates.

(F) Western blot for MYCN in SHEP21N cells with or without doxycycline treatment.

(G) Real-time cytotoxicity assay for IMP-1088 in high- and low-MYCN SHEP21N cells. A representative biological replicate is shown as mean ± SEM of *n* = 3 technical replicates. Figure 2A was created in BioRender. Zhang, J. (2025) https://BioRender.com/hsua0et. See also Figure S2 and Table S1.
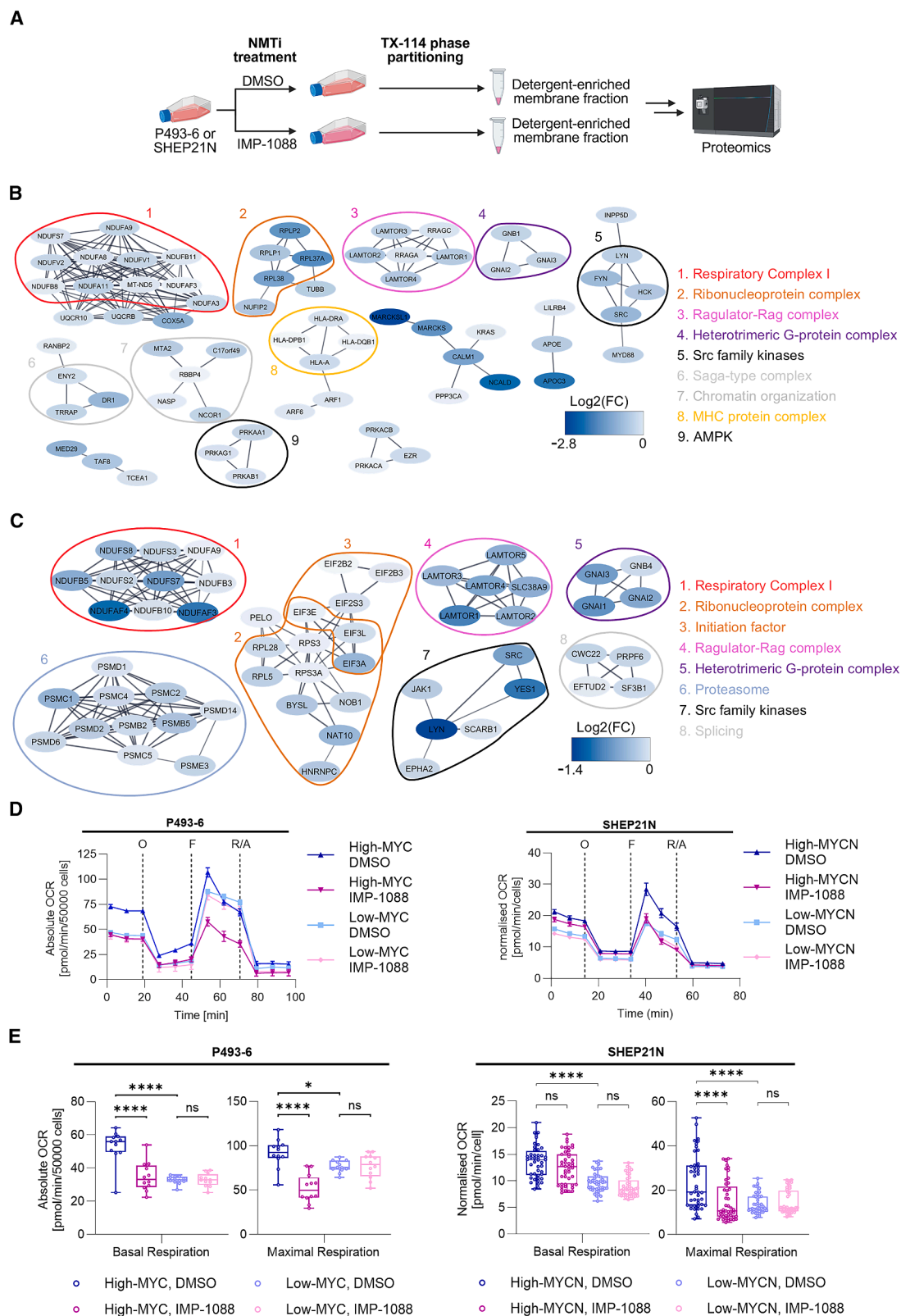
(legend on next page)

patient-derived (PD) LY11212 DLBCL cancer cells[57] (Figure S3G). PD LY11212 cells were derived from a patient with multi-chemotherapy-resistant lymphoma carrying *MYC* and *BCL2* translocations, characteristic of so-called "double hit" lymphomas that have the least favorable clinical outcomes among DLBCL.[58] In these cells, both IMP-1088 and DDD86481 delivered potent inhibition of *N*-myristoylation[39] (Figure S3H). Taken together, these findings indicate that NMTi drives mitochondrial respiratory complex I defects and subsequent mitochondrial dysfunction in MYC-deregulated cancer cells.

NMTi impacts NDUFAF4-associated complex I assembly in high-MYC cells

Deep proteomic analysis of the fractionated mitochondrial proteome in high- and low-MYC P493-6 cells with or without 100 nM IMP-1088 treatment revealed quantitative depletion of specific complex I proteins,[59] with NMTi only in high but not in low-MYC cells (Figures 4A and 4B), including NDUFAF4 and NDUFB7, which were previously shown to be human NMT substrates.[9,60] We chose to focus on NDUFAF4 as it is significantly and specifically depleted in the mitochondrial proteome in high-MYC cells treated with NMTi (Figure 4B) and in total protein extracts in both our MYC- and MYCN-inducible cell systems (Figures 4C and 4D). NDUFAF4 is a complex I assembly factor important for complex I expression and activity[61] and is directly transcriptionally regulated by MYC[62] and MYCN (Figure S4A). Notably, non-*N*-myristoylated NDUFAF4 is subject to degradation via the glycine N-degron pathway.[7] Furthermore, patients carrying a single Ala3Pro mutation in NDUFAF4 were recently reported to suffer a specific mitochondrial complex I assembly defect, leading to onset of Leigh syndrome.[63] We hypothesized that this mutation adjacent to the Gly2 *N*-myristoylation site phenocopies the impact of NMTi by abolishing NDUFAF4 *N*-myristoylation, leading to its proteasomal degradation through the glycine N-degron pathway. We expressed wild-type NDUFAF4 or NDUFAF4[Ala3Pro] with a C-terminal FLAG tag in HEK293 cells and found that NDUFAF4[Ala3Pro] expression was significantly reduced relative to wild type, which could be rescued by proteasome inhibition (Figure 4E). Furthermore, we found that NDUFAF4[Ala3Pro] N-terminal peptide is not a substrate for recombinant human NMT, in contrast to efficient *N*-myristoylation of wild-type NDUFAF4 peptide (Figure S4B), and NDUFAF4, but not NDUFAF4[Ala3Pro], protein could be metabolically labeled with myristate analogue YnMyr[39] in HEK293 cells (Figure S4C). Notably, the impact of NMTi on mitochondrial localization of complex I components in high-MYC P493-6 cells (Figure 4B) is

clustered around the Q module, which is dependent on NDUFAF4 for incorporation into complex I[59] (Figure 4F; Figure S4D), supporting the hypothesis that impaired NDUFAF4 *N*-myristoylation upon NMTi leads to specific complex I assembly defects in high MYC cells. Taken together, these data suggest that failure to *N*-myristoylated NDUFAF4 is sufficient to impair physiological complex I assembly in humans, as seen in patients with Leigh syndrome bearing the NDUFAF4 [Ala3Pro] mutation.

NMTi suppresses *MYC*- and *MYCN*-driven tumors

We next examined the *in vivo* impact of NMTi in a double-hit DLBCL model. DoHH2 cells were engrafted subcutaneously into CB17/SCID mice to establish tumors to a volume of 100–150 mm^3. Mice were treated with vehicle or IMP-1320 (Figure S5) at 25 mg/kg/day delivered intraperitoneally (i.p.) at 12.5 mg/kg BID using a 3 days on/3 days off dosing schedule. NMTi treatment resulted in significant tumor regression, with minimal residual tumor present at day 22 of the experiment, while tumors grew in all vehicle-treated controls (Figure 5A). No significant effect on body weight was observed, suggesting that IMP-1320 was well tolerated under this dosing schedule (Figure 5B). IMP-1320 was also efficacious in an immune-competent neuroblastoma mouse model. The TH-*MYCN* genetically engineered mouse (GEM) model spontaneously develop tumors and model *MYCN*-amplified neuroblastoma.[64] TH-*MYCN* tumor cells were engrafted into 129SvJ mice to establish a syngeneic model, and tumors were allowed to grow to ca. 5 mm in diameter, after which mice were treated with IMP-1320 at 25 mg/kg QD (i.p.) or vehicle on a 3 days on/4 days off schedule. IMP-1320 treatment resulted in strong tumor regression without obvious toxicity (Figures 5C and 5D). Notably, proteomic analyses of tumors following 3-day initial NMTi treatment revealed a significant reduction of mitochondrial respiratory complex I proteins compared to vehicle controls, in both DoHH2 xenograft and TH-*MYCN* GEM mice (Figure 5E). Meta-analysis further confirmed that this was the most significantly downregulated protein complex in both mouse models (Figure 5F). Furthermore, DDD86481 (Figure S6) profoundly inhibited tumor growth in NOD *scid* gamma (IL2R-NSG) mice subcutaneously injected with PD LY11212 cells (Figures S7A and S7B), which are highly sensitive to both IMP-1088 (EC$_{50}$ 5 nM) and DDD86481 (EC$_{50}$ 16 nM) *in vitro* (Figure S7C). Taken together, these data are consistent with the hypothesis that NMTi treatment could be efficacious in a range of MYC- or MYCN-driven cancers.

Figure 3. NMT inhibition induces depletion of biological nodes in detergent-enriched membrane fractions and severely impairs mitochondrial respiration in MYC- and MYCN-deregulated cells

(A) Schematic of experimental design. High MYC or MYCN cells were treated with IMP-1088 (P493-6: 100 nM, 24 h; SHEP21N: 50 nM, 18 h) or DMSO control. Detergent fractions were isolated by phase partitioning and processed for LC-MS/MS as described in the STAR Methods section.

(B and C) Protein-protein interaction network retrieved by STRING (STRING score >0.7) of depleted proteins in detergent fractions in high-MYC P493-6 cells (B) or high-MYCN SHEP21N cells (C) upon IMP-1088 treatment.

(D) Oxygen consumption rate (OCR) of P493-6 and SHEP21N cells expressing high and low MYC or MYCN levels upon treatment with IMP-1088 (100 nM, 18 h) or DMSO control. O, oligomycin; F, FCCP; R/A, rotenone and antimycin A. Data are shown as mean ± SEM of $n = 3$ biological replicates.

(E) Basal and maximal mitochondrial respiration in P493-6 and SHEP21N cells calculated using data from (D). Data are shown as mean ± SEM of $n = 3$ biological replicates. Significance was calculated by two-way ANOVA. ns: not statistically significant; $*p < 0.05$, $**p < 0.01$, $***p < 0.001$, $****p < 0.0001$. Figure 3A was created in BioRender. Zhang, J. (2025) https://BioRender.com/7nfx46o. See also Figure S3.
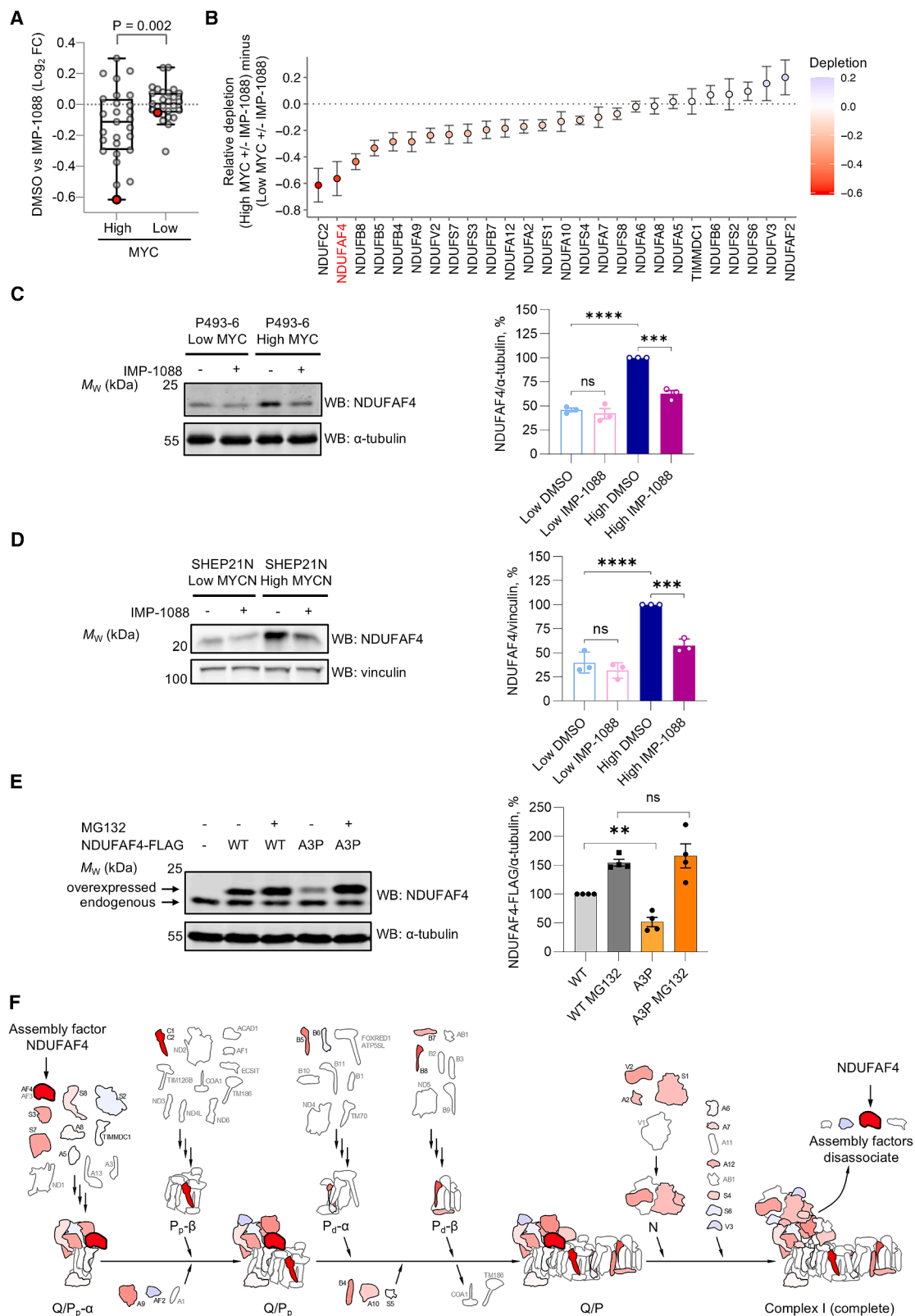
DISCUSSION

In this study, we identified that MYC-deregulated cancers are particularly sensitive to NMTi in a 245-cell-line screen. Although expression of NMT enzymes does not predict sensitivity, consistent with screens against other NMTi,[23] the effects of NMTi in cells are predominantly attributed to inhibition of NMT1, given that NMT1, but not NMT2, KO in HeLa cells greatly increased sensitivity to NMTis (Figure 1E). A small increase in sensitivity (<2-fold) was recently reported in HAP1 cells (a haploid model of chronic myelogenous leukemia [CML]) upon NMT2 KO, although consistent with our data the effect of NMT1 KO was much greater.[23] Importantly, the impact of MYC or MYCN deregulation on NMTi-induced cell death was verified in two distinct isogenic cell models, consistent with the sensitivity of MYC deregulation across cancer types (Figures 2E and 2G).

N-myristoylation is well known to direct substrates to the membrane to regulate multiple signaling pathways, and we describe here a systems-level analysis of the impact of NMTi in detergent-enriched membrane fractions (Figure 3). Our proteomics data are consistent with previous studies in NMT biology that connect NMT substrates such as LAMTOR1[12,13] and Src[23,47,66] to NMT inhibition, while also highlighting respiratory complex I as a highly affected node, as suggested by previous global analyses.[19,23] Differences in affected complexes upon NMTi were seen between each cell line investigated, such as the proteasome, a subpopulation of which is thought to rely on N-myristoylation for membrane association.[14] These differences may arise due to the different cell lineages of the two models or through differences between the cellular states induced by MYC and MYCN, respectively.

Mitochondrial dysfunction is both a hallmark and a liability of MYC deregulation,[67] and we show that the impact of NMTi on mitochondria is both robust and MYC-dependent, as measured by mitochondrial respiration and mitochondrial proteomics analyses. NDUFAF4 is a direct target of NMT and a direct transcriptional target of MYC, and we hypothesized that its N-myristoylation is important for NDUFAF4 expression and subsequent complex I assembly. Indeed, we found that NMTi treatment phenocopied a pathogenic A3P NDUFAF4 mutant, which is not

N-myristoylated and sufficient to drive physiological complex I defects in human patients with Leigh syndrome[63] (Figure 4). Moreover, NMTi-induced mitochondrial dysfunction and loss of complex I has also been reported in lymphoma models, including acute myeloid leukemia (AML) cell lines[47] and HAP1 cells,[23] although we show here the significant role of MYC deregulation on this phenotype. The differential responses driven by MYC modulation revealed in our study may arise from lower NDUFAF4 expression and turnover in low-MYC contexts. However, it is clear that the mechanisms by which NMTi induces cancer cell death are complex and perturbations in multiple cellular pathways occur simultaneously. As such, it is likely that contributions from several affected pathways combine to drive enhanced anticancer activity, as recently proposed.[17]

In addition to its effects on mitochondria and complex I, a major function of MYC is to drive general protein synthesis.[27] As N-myristoylation is an irreversible and predominantly co-translational modification,[1] the response of a cell to an NMTi is intrinsically linked to NMT substrate turnover.[17] It is therefore possible that MYC deregulation also sensitizes cancer cells to NMTi through its effects on proteome dynamics. Such activity would also be consistent with previous reports in *Drosophila* identifying *Nmt* as required for *Myc*-driven growth, with *Nmt* knockdown likely inducing ribosomal stress,[68] although the synthetic lethality observed here for NMTi is both more selective and more potent than for inhibitors of previously reported protein-synthesis-related targets in high-MYC cells.[69]

Our data are consistent with NMTi being highly effective in cancers in which MYC or MYCN is a driver oncogene, and indeed NMT1, but not NMT2, was recently identified in a genetic screen as a potential synthetic lethal knockout in combination with MYC overexpression.[70] The promising *in vitro* results in which highly MYC expressing cells were sensitized to IMP1088 translated well to our *in vivo* models of lymphoma and neuroblastoma, in which IMP-1320, an analogue of IMP-1088 with improved pharmacokinetic properties, robustly eliminated or controlled tumors. Furthermore, although we focused here on MYC, other Hallmark gene sets were also predictive for NMTi sensitivity (Figure S2A). These mostly overlapped with gene sets enriched in other analyses of NMTi sensitivity,[23] supporting

---

Figure 4. NMT inhibition leads to proteasomal degradation of complex I assembly factor NDUFAF4 in high-MYC cells

(A) Changes in abundance induced by NMTi for mitochondrial respiratory complex I proteins identified in mitochondria isolated from high- and low-MYC P493-6 cells treated with IMP-1088 (100 nM, 18 h) or DMSO vehicle (n = 27); NDUFAF4 highlighted in red. Tukey boxplot, significance calculated by Student's t test (two-tailed, heteroscedastic).

(B) Ranked responses of complex I proteins to IMP-1088 in high- vs. low-MYC P493-6 cells, color-graded by differential depletion. Data are shown as mean ± SD of n = 3 biological replicates.

(C and D) Western blot analysis of NDUFAF4 in low- or high-MYC P493-6 (C) or low- and high-MYCN SHEP21N (D) cells with and without IMP-1088 treatment (100 nM, 18 h). α-tubulin and vinculin were used as a loading control. For quantification, normalization was performed by dividing the NDUFAF4 antibody signal by the α-tubulin or vinculin antibody signal. The image for NDUFAF4 has been contrast adjusted from the original (min-max range set to 907–20049) to improve legibility using ImageJ; see Figure S8 for the original image data.

(E) Western blot analysis of C-terminally FLAG-tagged NDUFAF4 (WT and A3P mutant) expressed in HEK293 cells. MG132 (10 μM) was used to inhibit the proteasome. α-tubulin was used as a loading control. For quantification, normalization was performed by dividing the NDUFAF4 antibody signal by the α-tubulin antibody signal.

(F) Cartoon representation of the assembly pathway of human mitochondrial respiratory complex I adapted from ref. [59], with each identified subunit colored according to the impact of NMTi in high- vs. medium-MYC P493-6 cells, as calculated in (B) (unidentified subunits in gray). NDUFAF4 is highlighted. Subunit names shortened by omitting "NDUF." Data in (C and D) are shown as mean ± SEM of n = 3 biological replicates. Data in (E) are shown as mean ± SEM of n = 4 biological replicates. Significance was calculated by Student's t test (two-tailed, unpaired). ns: not statistically significant; *p < 0.05, **p < 0.01, ***p < 0.001, ****p < 0.0001. See also Figure S4.
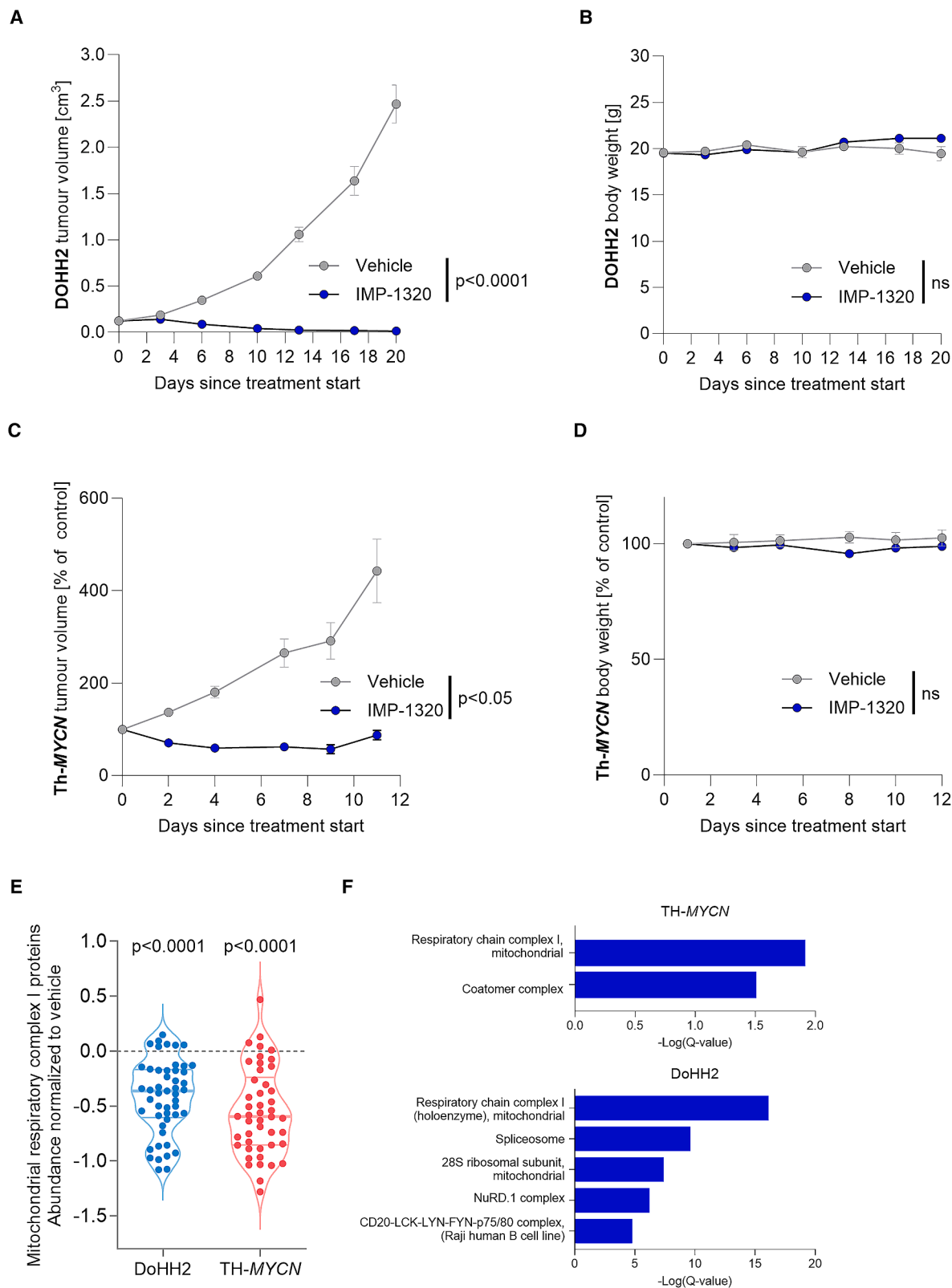
(legend on next page)

their biological relevance, and it is plausible that oncogenic deregulation of these pathways would also render cancer cells acutely sensitive to NMTi. Investigation of these pathways, as well as further characterizing the interplay between NMTi and MYC, would be useful in expanding our knowledge of the range of cancers in which NMTi may be most efficacious.

The advent of potent human NMTi has been essential to facilitate robust screening and system-level studies and to establish novel markers for NMTi sensitivity in cancer. NMT inhibitors have recently advanced to the clinic, and the results of a phase I trial of a NMTi have been reported.[71] NMTi was shown to be tolerated in patients at predicted efficacious doses, although the extent of clinical benefit remains to be determined, and dose-limiting toxicities were also identified. Successful application of systemic NMTi in the clinic may require biomarker-based identification of the most sensitive cancers to NMTi, as the diverse effects on >200 NMT substrates may lead to a relatively low therapeutic index for small molecule approaches.[17] Our data suggest that a significant therapeutic window exists to target MYC-driven cancers with NMTi, and we expect that future refinement of dose schedules and understanding of dose-limiting toxicity will enable clinical development of NMTi targeting high-MYC cancers. An alternative approach of targeted delivery, for example, through an NMTi antibody-drug conjugate (ADC) may offer an optimal balance between high efficacy and minimal toxicity and expand the range of treatable cancers, as recently reported (https://doi.org/10.1158/1538-7445.AM2023-2635).

Limitations of the study

In this study, we focused on the MYC-dependent effects of NMT inhibition through the lens of a single substrate, the complex I assembly factor NDUFAF4. While this mechanistic link provides a compelling rationale for selective sensitivity in MYC-deregulated cancers, we did not systematically assess whether other NMT substrates or the pathways they regulate are similarly affected in an MYC-dependent manner. Given the profound impact of MYC on protein synthesis and turnover, it is plausible that MYC deregulation sensitizes multiple pathways downstream of NMT by driving more rapid depletion of NMT substrates, but this hypothesis was not directly assessed in our study. Multiple pathways beyond complex I assembly have previously been proposed to modulate NMTi sensitivity in cancer, and future studies employing unbiased proteomic and functional screening approaches may uncover the broader network of MYC-sensitized NMT substrates and their contributions to NMTi-induced cytotoxicity.

While NMTi is highly effective *in vivo* in animal models of cancers with deregulated MYC, we did not assess the influence of

sex on the response to NMT inhibition. We also did not explore the durability of these responses, which may be relevant to MYC-deregulated cancers that often relapse following initial treatment. Extended *in vivo* studies could be undertaken to evaluate the potential for tumor recurrence after NMTi therapy, although in practice the value of animal studies for translation to humans remains limited. Such insights will help define the therapeutic window and inform the rational design of biomarker-driven or targeted delivery strategies for NMTi-based therapies.

Figure 5. NMT inhibition abolishes tumor growth *in vivo*

(A) Impact of intraperitoneally administered IMP-1320 (25 mg/kg/day dosed at 12.5 mg/kg BID) on the growth of DoHH2 cancer cells *in vivo*.

(B) Change in mouse body weight between the start and endpoint of the experiments for the DoHH2 xenograft, comparing treated and control.

(C) Impact of intraperitoneally administered IMP-1320 (25 mg/kg/day dosed QD) on the growth of TH-*MYCN* cancer cells in the syngeneic *in vivo* model.

(D) Change in mouse body weight between the start and endpoint of the experiments for the TH-*MYCN* syngeneic mice, comparing treated and control.

(E) Violin plot depicting NMTi-driven abundance changes, normalized to vehicle, observed for mitochondrial respiratory complex I proteins in tumors from DoHH2 xenograft and TH-*MYCN* GEM mice. Tumor proteomes were analyzed following 3 days of IMP-1320 treatment.

(F) Protein complexes most significantly enriched in proteins downregulated in TH-*MYCN* or DoHH2 tumors following 3 days of IMP-1320 treatment. Complexes were retrieved from CORUM.[65] Data in (A–D) are shown as mean ± SEM. Significance was calculated by repeated-measures ANOVA in (A), repeated-measures mixed-effect analysis in (B–D), and the non-parametric, paired Wilcoxon t test in (E). ns: not statistically significant. See also Figures S5–S7.

AUTHOR CONTRIBUTIONS

E.W.T. and D.P.C. conceptualized the study. G.A.L. performed data analysis on Sanger Project Score, Cancer Dependency Map, and DepMap data and performed FACS experiments for the P493-6 line. J.Z. performed all experiments for the SHEP21N cell line, analyzed TX-114 fractionated data and *in vivo* proteomics data, and contributed to manuscript writing. M.F. generated CRISPR-Cas9 knockout of NMT1/2 in HeLa cells, performed FACS experiments for the MYCN-ER-SHEP line, metabolic viability for PDX with DDD86841, mitochondrial potential and ROS assays, and carried out *in vivo* mouse experiments with The Francis Crick Institute Biological Research Facility. A.G. performed *in vitro* and cellular NMTi inhibition assays, YnMyr profiling by in-gel fluorescence, Seahorse mitochondrial analysis, NDUFAF4 cloning, mutagenesis, expression, and biochemical experiments and contributed to manuscript writing. W.W.K. performed mitochondrial fractionation, complex I proteomic analysis, and deep proteomics of DoHH2 and TH-*MYCN* tumors and contributed to manuscript writing. F.F. developed and applied the data analysis pipelines for the cell line panel. J.W. performed real-time cytotoxicity assays and TX114-enrichment proteomics preparation for the P493-6 cell line. J.W.H. developed and optimized Tims-Tof running conditions and data processing pipelines and assisted with the development of the TX-114 enrichment protocol and data analysis. S.V. performed MYC expression experiments and assisted with TX-114 enrichment proteomics preparation in P493-6 cells. E.P. and B.M.C. carried out *in vivo* TH-MYCN syngeneic mouse experiments. R.S. and R.C. provided data on DoHH2 *in vivo* experiments. A.S.B. designed IMP-1320. E.J.B. purified NMT1 and NMT2 and performed S.P.R. and C.P.M. experiments. B.B. and M.J. generated and provided the B cell lymphoma PDX LY11212 cell line. E.W.T., D.P.C., and L.C. supervised the study and secured funding. E.W.T. wrote the manuscript, with input from all authors.

DECLARATION OF INTERESTS

STAR★METHODS

Detailed methods are provided in the online version of this paper and include the following:

- KEY RESOURCES TABLE
- EXPERIMENTAL MODEL AND STUDY PARTICIPANT DETAILS
  - Cell lines
  - Mouse models
- METHOD DETAILS
  - Enzymatic NMT assays
  - Cell line panel
  - Cell line screen analysis
  - Cloning
  - Generation of NMT1 and NMT2 CRISPR-Cas9 knockout clones in HeLa cells
  - Verification of CRISPR-Cas9 knockouts by sequencing
  - NMTi treatment
  - Real-time cytotoxicity assay
  - Western Blot
  - TX-114 fractionated proteomics
  - Data-dependent acquisition
  - Data-independent acquisition
  - Proteomics data analysis
  - Oxygen consumption rate measurements
  - Mitochondrial proteomics
  - Mitochondrial proteomics analysis
  - NDUFAF4 biochemistry
  - *In vivo* proteomics
  - Meta-analysis
  - SPR
  - Public datasets
  - YnMyr labeling for in-gel fluorescence and streptavidin pulldown
  - Cell viability measurements
  - Flow cytometry
  - Cytofluorimetry for MitoTracker staining
- QUANTIFICATION AND STATISTICAL ANALYSIS

SUPPLEMENTAL INFORMATION

Supplemental information can be found online at https://doi.org/10.1016/j.celrep.2025.116180.

REFERENCES

1. Meinnel, T., Dian, C., and Giglione, C. (2020). Myristoylation, an Ancient Protein Modification Mirroring Eukaryogenesis and Evolution. Trends Biochem. Sci. *45*, 619–632. https://doi.org/10.1016/j.tibs.2020.03.007.

2. Glover, C.J., Hartman, K.D., and Felsted, R.L. (1997). Human N-Myristoyltransferase Amino-terminal Domain Involved in Targeting the Enzyme to the Ribosomal Subcellular Fraction. J. Biol. Chem. *272*, 28680–28689. https://doi.org/10.1074/jbc.272.45.28680.

3. Rampoldi, F., Bonrouhi, M., Boehm, M.E., Lehmann, W.D., Popovic, Z.V., Kaden, S., Federico, G., Brunk, F., Gröne, H.-J., and Porubsky, S. (2015). Immunosuppression and Aberrant T Cell Development in the Absence of N-Myristoylation. J. Immunol. *195*, 4228–4243. https://doi.org/10.4049/jimmunol.1500622.

4. Yang, S.H., Shrivastav, A., Kosinski, C., Sharma, R.K., Chen, M.-H., Berthiaume, L.G., Peters, L.L., Chuang, P.-T., Young, S.G., and Bergo, M.O. (2005). N-Myristoyltransferase 1 Is Essential in Early Mouse Development. J. Biol. Chem. *280*, 18990–18995. https://doi.org/10.1074/jbc.m412917200.

5. Doll, S., Freitas, F.P., Shah, R., Aldrovandi, M., Da Silva, M.C., Ingold, I., Goya Grocin, A., Xavier Da Silva, T.N., Panzilius, E., Scheel, C.H., et al. (2019). FSP1 is a glutathione-independent ferroptosis suppressor. Nature *575*, 693–698. https://doi.org/10.1038/s41586-019-1707-0.

6. Dian, C., Pérez-Dorado, I., Rivière, F., Asensio, T., Legrand, P., Ritzefeld, M., Shen, M., Cota, E., Meinnel, T., Tate, E.W., and Giglione, C. (2020). High-resolution snapshots of human N-myristoyltransferase in action

illuminate a mechanism promoting N-terminal Lys and Gly myristoylation. Nat. Commun. *11*, 1132. https://doi.org/10.1038/s41467-020-14847-3.

7. Timms, R.T., Zhang, Z., Rhee, D.Y., Harper, J.W., Koren, I., and Elledge, S. J. (2019). A glycine-specific N-degron pathway mediates the quality control of protein *N*-myristoylation. Science *365*, eaaw4912. https://doi.org/10.1126/science.aaw4912.

8. Zhu, X.G., Nicholson Puthenveedu, S., Shen, Y., La, K., Ozlu, C., Wang, T., Klompstra, D., Gultekin, Y., Chi, J., Fidelin, J., et al. (2019). CHP1 Regulates Compartmentalized Glycerolipid Synthesis by Activating GPAT4. Mol. Cell *74*, 45–58.e7. https://doi.org/10.1016/j.molcel.2019.01.037.

9. Thinon, E., Serwa, R.A., Broncel, M., Brannigan, J.A., Brassat, U., Wright, M.H., Heal, W.P., Wilkinson, A.J., Mann, D.J., and Tate, E.W. (2014). Global profiling of co- and post-translationally N-myristoylated proteomes in human cells. Nat. Commun. *5*, 4919. https://doi.org/10.1038/ncomms5919.

10. Tate, E.W., Kalesh, K.A., Lanyon-Hogg, T., Storck, E.M., and Thinon, E. (2015). Global profiling of protein lipidation using chemical proteomic technologies. Curr. Opin. Chem. Biol. *24*, 48–57. https://doi.org/10.1016/j.cbpa.2014.10.016.

11. Castrec, B., Dian, C., Ciccone, S., Ebert, C.L., Bienvenut, W.V., Le Caer, J.-P., Steyaert, J.-M., Giglione, C., and Meinnel, T. (2018). Structural and genomic decoding of human and plant myristoylomes reveals a definitive recognition pattern. Nat. Chem. Biol. *14*, 671–679. https://doi.org/10.1038/s41589-018-0077-5.

12. Chen, Y.-C., Navarrete, M.S., Wang, Y., McClintock, N.C., Sakurai, R., Wang, F., Chen, K.T., Chou, T.-F., Rehan, V.K., Lee, D.J., and Diaz, B. (2020). N-myristoyltransferase-1 is necessary for lysosomal degradation and mTORC1 activation in cancer cells. Sci. Rep. *10*, 11952. https://doi.org/10.1038/s41598-020-68615-w.

13. Sun, Y., Guan, Z., Sheng, Q., Duan, W., Zhao, H., Zhou, J., Deng, Q., and Pei, X. (2022). N-myristoyltransferase-1 deficiency blocks myristoylation of LAMTOR1 and inhibits bladder cancer progression. Cancer Lett. *529*, 126–138. https://doi.org/10.1016/j.canlet.2022.01.001.

14. Zhang, R., Pan, S., Zheng, S., Liao, Q., Jiang, Z., Wang, D., Li, X., Hu, A., Li, X., Zhu, Y., et al. (2023). Lipid-anchored proteasomes control membrane protein homeostasis. Sci. Adv. *9*, eadj4605. https://doi.org/10.1126/sciadv.adj4605.

15. McHugh, D., Sun, B., Gutierrez-Muñoz, C., Hernández-González, F., Mellone, M., Guiho, R., Duran, I., Pombo, J., Pietrocola, F., Birch, J., et al. (2023). COPI vesicle formation and N-myristoylation are targetable vulnerabilities of senescent cells. Nat. Cell Biol. *25*, 1804–1820. https://doi.org/10.1038/s41556-023-01287-6.

16. Luo, P.M., and Boyce, M. (2019). Directing Traffic: Regulation of COPI Transport by Post-translational Modifications. Front. Cell Dev. Biol. *7*, 190. https://doi.org/10.3389/fcell.2019.00190.

17. Tate, E.W., Soday, L., De La Lastra, A.L., Wang, M., and Lin, H. (2024). Protein lipidation in cancer: mechanisms, dysregulation and emerging drug targets. Nat. Rev. Cancer *24*, 240–260. https://doi.org/10.1038/s41568-024-00666-x.

18. Sondka, Z., Bamford, S., Cole, C.G., Ward, S.A., Dunham, I., and Forbes, S.A. (2018). The COSMIC Cancer Gene Census: describing genetic dysfunction across all human cancers. Nat. Rev. Cancer *18*, 696–705. https://doi.org/10.1038/s41568-018-0060-1.

19. Thinon, E., Morales-Sanfrutos, J., Mann, D.J., and Tate, E.W. (2016). *N*-Myristoyltransferase Inhibition Induces ER-Stress, Cell Cycle Arrest, and Apoptosis in Cancer Cells. ACS Chem. Biol. *11*, 2165–2176. https://doi.org/10.1021/acschembio.6b00371.

20. Kallemeijn, W.W., Lueg, G.A., Faronato, M., Hadavizadeh, K., Goya Grocin, A., Song, O.-R., Howell, M., Calado, D.P., and Tate, E.W. (2019). Validation and Invalidation of Chemical Probes for the Human N-myristoyltransferases. Cell Chem. Biol. *26*, 892–900.e4. https://doi.org/10.1016/j.chembiol.2019.03.006.

21. Mousnier, A., Bell, A.S., Swieboda, D.P., Morales-Sanfrutos, J., Pérez-Dorado, I., Brannigan, J.A., Newman, J., Ritzefeld, M., Hutton, J.A., Guedán, A., et al. (2018). Fragment-derived inhibitors of human N-myristoyltransferase block capsid assembly and replication of the common cold virus. Nat. Chem. *10*, 599–606. https://doi.org/10.1038/s41557-018-0039-2.

22. Beauchamp, E., Yap, M.C., Iyer, A., Perinpanayagam, M.A., Gamma, J.M., Vincent, K.M., Lakshmanan, M., Raju, A., Tergaonkar, V., Tan, S.Y., et al. (2020). Targeting N-myristoylation for therapy of B-cell lymphomas. Nat. Commun. *11*, 5348. https://doi.org/10.1038/s41467-020-18998-1.

23. Beauchamp, E., Gamma, J.M., Cromwell, C.R., Moussa, E.W., Pain, R., Kostiuk, M.A., Acevedo-Morantes, C., Iyer, A., Yap, M., Vincent, K.M., et al. (2024). Multiomics analysis identifies oxidative phosphorylation as a cancer vulnerability arising from myristoylation inhibition. J. Transl. Med. *22*, 431. https://doi.org/10.1186/s12967-024-05150-6.

24. Tate, E., and Bell, A.S. (2020). NOVEL COMPOUNDS AND THEIR USE IN THERAPY. patent application WO2020128473A1.

25. Brand, S., Norcross, N.R., Thompson, S., Harrison, J.R., Smith, V.C., Robinson, D.A., Torrie, L.S., McElroy, S.P., Hallyburton, I., Norval, S., et al. (2014). Lead Optimization of a Pyrazole Sulfonamide Series of *Trypanosoma brucei* N-Myristoyltransferase Inhibitors: Identification and Evaluation of CNS Penetrant Compounds as Potential Treatments for Stage 2 Human African Trypanosomiasis. J. Med. Chem. *57*, 9855–9869. https://doi.org/10.1021/jm500809c.

26. Dang, C.V. (2012). MYC on the Path to Cancer. Cell *149*, 22–35. https://doi.org/10.1016/j.cell.2012.03.003.

27. Gabay, M., Li, Y., and Felsher, D.W. (2014). MYC Activation Is a Hallmark of Cancer Initiation and Maintenance. Cold Spring Harb. Perspect. Med. *4*, a014241. https://doi.org/10.1101/cshperspect.a014241.

28. Wolf, E., and Eilers, M. (2020). Targeting MYC Proteins for Tumor Therapy. Annu. Rev. Cancer Biol. *4*, 61–75. https://doi.org/10.1146/annurev-cancerbio-030518-055826.

29. Chen, H., Liu, H., and Qing, G. (2018). Targeting oncogenic Myc as a strategy for cancer treatment. Signal Transduct. Target. Ther. *3*, 5. https://doi.org/10.1038/s41392-018-0008-7.

30. McKeown, M.R., and Bradner, J.E. (2014). Therapeutic Strategies to Inhibit MYC. Cold Spring Harb. Perspect. Med. *4*, a014266. https://doi.org/10.1101/cshperspect.a014266.

31. Meyers, R.M., Bryan, J.G., McFarland, J.M., Weir, B.A., Sizemore, A.E., Xu, H., Dharia, N.V., Montgomery, P.G., Cowley, G.S., Pantel, S., et al. (2017). Computational correction of copy number effect improves specificity of CRISPR–Cas9 essentiality screens in cancer cells. Nat. Genet. *49*, 1779–1784. https://doi.org/10.1038/ng.3984.

32. Behan, F.M., Iorio, F., Picco, G., Gonçalves, E., Beaver, C.M., Migliardi, G., Santos, R., Rao, Y., Sassi, F., Pinnelli, M., et al. (2019). Prioritization of cancer therapeutic targets using CRISPR–Cas9 screens. Nature *568*, 511–516. https://doi.org/10.1038/s41586-019-1103-9.

33. Dempster, J.M., Pacini, C., Pantel, S., Behan, F.M., Green, T., Krill-Burger, J., Beaver, C.M., Younger, S.T., Zhivich, V., Najgebauer, H., et al. (2019). Agreement between two large pan-cancer CRISPR-Cas9 gene dependency data sets. Nat. Commun. *10*, 5817. https://doi.org/10.1038/s41467-019-13805-y.

34. Bell, A.S., Mills, J.E., Williams, G.P., Brannigan, J.A., Wilkinson, A.J., Parkinson, T., Leatherbarrow, R.J., Tate, E.W., Holder, A.A., and Smith, D.F. (2012). Selective Inhibitors of Protozoan Protein N-myristoyltransferases as Starting Points for Tropical Disease Medicinal Chemistry Programs. PLoS Negl. Trop. Dis. *6*, e1625. https://doi.org/10.1371/journal.pntd.0001625.

35. Barbie, D.A., Tamayo, P., Boehm, J.S., Kim, S.Y., Moody, S.E., Dunn, I.F., Schinzel, A.C., Sandy, P., Meylan, E., Scholl, C., et al. (2009). Systematic RNA interference reveals that oncogenic KRAS-driven cancers require TBK1. Nature *462*, 108–112. https://doi.org/10.1038/nature08460.

36. Liberzon, A., Birger, C., Thorvaldsdóttir, H., Ghandi, M., Tamayo, P., Jill, and Mesirov, J. (2015). The Molecular Signatures Database Hallmark Gene Set Collection. Cell Syst. *1*, 417–425. https://doi.org/10.1016/j.cels.2015.12.004.

37. Barretina, J., Caponigro, G., Stransky, N., Venkatesan, K., Margolin, A.A., Kim, S., Wilson, C.J., Lehár, J., Kryukov, G.V., Sonkin, D., et al. (2012). The Cancer Cell Line Encyclopedia enables predictive modelling of anti-cancer drug sensitivity. Nature *483*, 603–607. https://doi.org/10.1038/nature11003.

38. Pajic, A., Spitkovsky, D., Christoph, B., Kempkes, B., Schuhmacher, M., Staege, M.S., Brielmeier, M., Ellwart, J., Kohlhuber, F., Bornkamm, G. W., et al. (2000). Cell cycle activation by c-myc in a Burkitt lymphoma model cell line. Int. J. Cancer *87*, 787–793. https://doi.org/10.1002/1097-0215(20000915)87:6<787::aid-ijc4>3.0.co;2-6.

39. Kallemeijn, W.W., Lanyon-Hogg, T., Panyain, N., Goya Grocin, A., Ciepla, P., Morales-Sanfrutos, J., and Tate, E.W. (2021). Proteome-wide analysis of protein lipidation using chemical probes: in-gel fluorescence visualization, identification and quantification of N-myristoylation, N- and S-acylation, O-cholesterylation, S-farnesylation and S-geranylgeranylation. Nat. Protoc. *16*, 5083–5122. https://doi.org/10.1038/s41596-021-00601-6.

40. Lutz, W., Stöhr, M., Schürmann, J., Wenzel, A., Löhr, A., and Schwab, M. (1996). Conditional expression of N-myc in human neuroblastoma cells increases expression of alpha-prothymosin and ornithine decarboxylase and accelerates progression into S-phase early after mitogenic stimulation of quiescent cells. Oncogene *13*, 803–812.

41. Valentijn, L.J., Koppen, A., Van Asperen, R., Root, H.A., Haneveld, F., and Versteeg, R. (2005). Inhibition of a New Differentiation Pathway in Neuroblastoma by Copy Number Defects of N-myc, Cdc42, and nm23 Genes. Cancer Res. *65*, 3136–3145. https://doi.org/10.1158/0008-5472.can-04-2469.

42. Schulte, J.H., Horn, S., Otto, T., Samans, B., Heukamp, L.C., Eilers, U.C., Krause, M., Astrahantseff, K., Klein-Hitpass, L., Buettner, R., et al. (2008). MYCN regulates oncogenic MicroRNAs in neuroblastoma. Int. J. Cancer *122*, 699–704. https://doi.org/10.1002/ijc.23153.

43. Fang, W., Robinson, D.A., Raimi, O.G., Blair, D.E., Harrison, J.R., Lockhart, D.E.A., Torrie, L.S., Ruda, G.F., Wyatt, P.G., Gilbert, I.H., and Van Aalten, D.M.F. (2015). *N*-Myristoyltransferase Is a Cell Wall Target in *Aspergillus fumigatus*. ACS Chem. Biol. *10*, 1425–1434. https://doi.org/10.1021/cb5008647.

44. Burnaevskiy, N., Peng, T., Reddick, L.E., Hang, H.C., and Alto, N.M. (2015). Myristoylome Profiling Reveals a Concerted Mechanism of ARF GTPase Deacylation by the Bacterial Protease IpaJ. Mol. Cell *58*, 110–122. https://doi.org/10.1016/j.molcel.2015.01.040.

45. Taguchi, Y., and Schätzl, H.M. (2014). Small-scale Triton X-114 Extraction of Hydrophobic Proteins. Bio. Protoc. *4*, e1139. https://doi.org/10.21769/bioprotoc.1139.

46. Doncheva, N.T., Morris, J.H., Gorodkin, J., and Jensen, L.J. (2019). Cytoscape StringApp: Network Analysis and Visualization of Proteomics Data. J. Proteome Res. *18*, 623–632. https://doi.org/10.1021/acs.jproteome.8b00702.

47. Gamma, J.M., Liu, Q., Beauchamp, E., Iyer, A., Yap, M.C., Zak, Z., Ekstrom, C., Pain, R., Kostiuk, M.A., Mackey, J.R., et al. (2025). Zelenirstat Inhibits N-Myristoyltransferases to Disrupt Src Family Kinase Signalling and Oxidative Phosphorylation Killing Acute Myeloid Leukemia Cells. Mol. Cancer Ther. *24*, 69–80. https://doi.org/10.1158/1535-7163.mct-24-0307.

48. Dang, C.V. (2013). MYC, Metabolism, Cell Growth, and Tumorigenesis. Cold Spring Harb. Perspect. Med. *3*, a014217. https://doi.org/10.1101/cshperspect.a014217.

49. Oliynyk, G., Ruiz-Pérez, M.V., Sainero-Alcolado, L., Dzieran, J., Zirath, H., Gallart-Ayala, H., Wheelock, C.E., Johansson, H.J., Nilsson, R., Lehtiö, J., and Arsenian-Henriksson, M. (2019). MYCN-enhanced Oxidative and Glycolytic Metabolism Reveals Vulnerabilities for Targeting Neuroblastoma. iScience *21*, 188–204. https://doi.org/10.1016/j.isci.2019.10.020.

50. Anderson, N.M., Qin, X., Finan, J.M., Lam, A., Athoe, J., Missiaen, R., Skuli, N., Kennedy, A., Saini, A.S., Tao, T., et al. (2021). Metabolic Enzyme DLST Promotes Tumor Aggression and Reveals a Vulnerability to OXPHOS Inhibition in High-Risk Neuroblastoma. Cancer Res. *81*, 4417–4430. https://doi.org/10.1158/0008-5472.can-20-2153.

51. D'Andrea, A., Gritti, I., Nicoli, P., Giorgio, M., Doni, M., Conti, A., Bianchi, V., Casoli, L., Sabò, A., Mironov, A., et al. (2016). The mitochondrial translation machinery as a therapeutic target in Myc-driven lymphomas. Oncotarget *7*, 72415–72430. https://doi.org/10.18632/oncotarget.11719.

52. Donati, G., Ravà, M., Filipuzzi, M., Nicoli, P., Cassina, L., Verrecchia, A., Doni, M., Rodighiero, S., Parodi, F., Boletta, A., et al. (2022). Targeting mitochondrial respiration and the BCL2 family in high-grade MYC-associated B-cell lymphoma. Mol. Oncol. *16*, 1132–1152. https://doi.org/10.1002/1878-0261.13115.

53. Oran, A.R., Adams, C.M., Zhang, X.-Y., Gennaro, V.J., Pfeiffer, H.K., Mellert, H.S., Seidel, H.E., Mascioli, K., Kaplan, J., Gaballa, M.R., et al. (2016). Multi-focal control of mitochondrial gene expression by oncogenic MYC provides potential therapeutic targets in cancer. Oncotarget *7*, 72395–72414. https://doi.org/10.18632/oncotarget.11718.

54. Bock, F.J., and Tait, S.W.G. (2020). Mitochondria as multifaceted regulators of cell death. Nat. Rev. Mol. Cell Biol. *21*, 85–100. https://doi.org/10.1038/s41580-019-0173-8.

55. Li, F., Wang, Y., Zeller, K.I., Potter, J.J., Wonsey, D.R., O'Donnell, K.A., Kim, J.-W., Yustein, J.T., Lee, L.A., and Dang, C.V. (2005). Myc Stimulates Nuclearly Encoded Mitochondrial Genes and Mitochondrial Biogenesis. Mol. Cell Biol. *25*, 6225–6234. https://doi.org/10.1128/mcb.25.14.6225-6234.2005.

56. Hartleben, G., Müller, C., Krämer, A., Schimmel, H., Zidek, L.M., Dornblut, C., Winkler, R., Eichwald, S., Kortman, G., Kosan, C., et al. (2018). Tuberous sclerosis complex is required for tumor maintenance in MYC-driven Burkitt's lymphoma. EMBO J. *37*, e98589. https://doi.org/10.15252/embj.201798589.

57. Li, L.-R., Wang, L., He, Y.-Z., and Young, K.H. (2019). Current perspectives on the treatment of double hit lymphoma. Expert Rev. Hematol. *12*, 507–514. https://doi.org/10.1080/17474086.2019.1623020.

58. Riedell, P.A., and Smith, S.M. (2018). Double hit and double expressors in lymphoma: Definition and treatment. Cancer *124*, 4622–4632. https://doi.org/10.1002/cncr.31646.

59. Guerrero-Castillo, S., Baertling, F., Kownatzki, D., Wessels, H.J., Arnold, S., Brandt, U., and Nijtmans, L. (2017). The Assembly Pathway of Mitochondrial Respiratory Chain Complex I. Cell Metab. *25*, 128–139. https://doi.org/10.1016/j.cmet.2016.09.002.

60. Harada, H., Moriya, K., Kobuchi, H., Ishihara, N., and Utsumi, T. (2023). Protein N-myristoylation plays a critical role in the mitochondrial localization of human mitochondrial complex I accessory subunit NDUFB7. Sci. Rep. *13*, 22991. https://doi.org/10.1038/s41598-023-50390-z.

61. Saada, A., Edvardson, S., Rapoport, M., Shaag, A., Amry, K., Miller, C., Lorberboum-Galski, H., and Elpeleg, O. (2008). C6ORF66 Is an Assembly Factor of Mitochondrial Complex I. Am. J. Hum. Genet. *82*, 32–38. https://doi.org/10.1016/j.ajhg.2007.08.003.

62. Seitz, V., Butzhammer, P., Hirsch, B., Hecht, J., Gütgemann, I., Ehlers, A., Lenze, D., Oker, E., Sommerfeld, A., Von Der Wall, E., et al. (2011). Deep Sequencing of MYC DNA-Binding Sites in Burkitt Lymphoma. PLoS One *6*, e26837. https://doi.org/10.1371/journal.pone.0026837.

63. Baertling, F., Sánchez-Caballero, L., Van Den Brand, M.A.M., Wintjes, L. T., Brink, M., Van Den Brandt, F.A., Wilson, C., Rodenburg, R.J.T., and Nijtmans, L.G.J. (2017). NDUFAF4 variants are associated with Leigh syndrome and cause a specific mitochondrial complex I assembly defect. Eur. J. Hum. Genet. *25*, 1273–1277. https://doi.org/10.1038/ejhg.2017.133.

64. Weiss, W.A., Aldape, K., Mohapatra, G., Feuerstein, B.G., and Bishop, J. M. (1997). Targeted expression of MYCN causes neuroblastoma in

transgenic mice. EMBO J. *16*, 2985–2995. https://doi.org/10.1093/emboj/16.11.2985.

65. Tsitsiridis, G., Steinkamp, R., Giurgiu, M., Brauner, B., Fobo, G., Frishman, G., Montrone, C., and Ruepp, A. (2023). CORUM: the comprehensive resource of mammalian protein complexes–2022. Nucleic Acids Res. *51*, D539–D545. https://doi.org/10.1093/nar/gkac1015.

66. Cross, F.R., Garber, E.A., Pellman, D., and Hanafusa, H. (1984). A Short Sequence in the p60*src* N Terminus Is Required for p60*src* Myristylation and Membrane Association and for Cell Transformation. Mol. Cell Biol. *4*, 1834–1842. https://doi.org/10.1128/mcb.4.9.1834-1842.1984.

67. Tameire, F., Verginadis, I.I., Leli, N.M., Polte, C., Conn, C.S., Ojha, R., Salas Salinas, C., Chinga, F., Monroy, A.M., Fu, W., et al. (2019). ATF4 couples MYC-dependent translational activity to bioenergetic demands during tumour progression. Nat. Cell Biol. *21*, 889–899. https://doi.org/10.1038/s41556-019-0347-9.

68. Zirin, J., Ni, X., Sack, L.M., Yang-Zhou, D., Hu, Y., Brathwaite, R., Bulyk, M.L., Elledge, S.J., and Perrimon, N. (2019). Interspecies analysis of MYC targets identifies tRNA synthetases as mediators of growth and survival in MYC-overexpressing cells. Proc. Natl. Acad. Sci. USA *116*, 14614–14619. https://doi.org/10.1073/pnas.1821863116.

69. Pourdehnad, M., Truitt, M.L., Siddiqi, I.N., Ducker, G.S., Shokat, K.M., and Ruggero, D. (2013). Myc and mTOR converge on a common node in protein synthesis control that confers synthetic lethality in Myc-driven cancers. Proc. Natl. Acad. Sci. USA *110*, 11988–11993. https://doi.org/10.1073/pnas.1310230110.

70. Martin, T.D., Choi, M.Y., Patel, R., Liang, A., Li, M.Z., and Elledge, S.J. (2024). Identification of MYC synthetic lethal genes and networks. Preprint at bioRxiv. https://doi.org/10.1101/2024.04.25.590465.

71. Sangha, R., Jamal, R., Spratlin, J., Kuruvilla, J., Sehn, L.H., Beauchamp, E., Weickert, M., Berthiaume, L.G., and Mackey, J.R. (2024). A first-in-human phase I trial of daily oral zelenirstat, a N-myristoyltransferase inhibitor, in patients with advanced solid tumors and relapsed/refractory B-cell lymphomas. Invest. New Drugs *42*, 386–393. https://doi.org/10.1007/s10637-024-01448-w.

72. Goncalves, V., Brannigan, J.A., Thinon, E., Olaleye, T.O., Serwa, R., Lanzarone, S., Wilkinson, A.J., Tate, E.W., and Leatherbarrow, R.J. (2012). A fluorescence-based assay for N-myristoyltransferase activity. Anal. Biochem. *421*, 342–344. https://doi.org/10.1016/j.ab.2011.10.013.

73. Broncel, M., Serwa, R.A., Ciepla, P., Krause, E., Dallman, M.J., Magee, A.I., and Tate, E.W. (2015). Multifunctional Reagents for Quantitative Proteome-Wide Analysis of Protein Modification in Human Cells and Dynamic Profiling of Protein Lipidation During Vertebrate Development. Angew. Chem. Int. Ed. Engl. *54*, 5948–5951. https://doi.org/10.1002/anie.201500342.

74. Zeid, R., Lawlor, M.A., Poon, E., Reyes, J.M., Fulciniti, M., Lopez, M.A., Scott, T.G., Nabet, B., Erb, M.A., Winter, G.E., et al. (2018). Enhancer invasion shapes MYCN-dependent transcriptional amplification in neuroblastoma. Nat. Genet. *50*, 515–523. https://doi.org/10.1038/s41588-018-0044-9.

75. Schneider, C.A., Rasband, W.S., and Eliceiri, K.W. (2012). NIH Image to ImageJ: 25 years of image analysis. Nat. Methods *9*, 671–675. https://doi.org/10.1038/nmeth.2089.

76. Cox, J., and Mann, M. (2008). MaxQuant enables high peptide identification rates, individualized p.p.b.-range mass accuracies and proteome-wide protein quantification. Nat. Biotechnol. *26*, 1367–1372. https://doi.org/10.1038/nbt.1511.

77. Demichev, V., Messner, C.B., Vernardis, S.I., Lilley, K.S., and Ralser, M. (2020). DIA-NN: neural networks and interference correction enable deep proteome coverage in high throughput. Nat. Methods *17*, 41–44. https://doi.org/10.1038/s41592-019-0638-x.

78. Cox, J., Hein, M.Y., Luber, C.A., Paron, I., Nagaraj, N., and Mann, M. (2014). Accurate Proteome-wide Label-free Quantification by Delayed Normalization and Maximal Peptide Ratio Extraction, Termed MaxLFQ. Mol. Cell. Proteomics *13*, 2513–2526. https://doi.org/10.1074/mcp.m113.031591.

79. Shannon, P., Markiel, A., Ozier, O., Baliga, N.S., Wang, J.T., Ramage, D., Amin, N., Schwikowski, B., and Ideker, T. (2003). Cytoscape: A Software Environment for Integrated Models of Biomolecular Interaction Networks. Genome Res. *13*, 2498–2504. https://doi.org/10.1101/gr.1239303.

80. Zhou, Y., Zhou, B., Pache, L., Chang, M., Khodabakhshi, A.H., Tanaseichuk, O., Benner, C., and Chanda, S.K. (2019). Metascape provides a biologist-oriented resource for the analysis of systems-level datasets. Nat. Commun. *10*, 1523. https://doi.org/10.1038/s41467-019-09234-6.

81. Ding, Q., Cowan, C.A., Musunuru, K., Stephanie, Regan, S.N., Leoníe, C., and Oostrom, L.A. (2013). Enhanced Efficiency of Human Pluripotent Stem Cell Genome Editing through Replacing TALENS with CRISPRs. Cell Stem Cell *12*, 393–394. https://doi.org/10.1016/j.stem.2013.03.006.

82. Labun, K., Montague, T.G., Krause, M., Torres Cleuren, Y.N., Tjeldnes, H., and Valen, E. (2019). CHOPCHOP v3: expanding the CRISPR web toolbox beyond genome editing. Nucleic Acids Res. *47*, W171–W174. https://doi.org/10.1093/nar/gkz365.

83. Van Den Ent, F., and Löwe, J. (2006). RF cloning: A restriction-free method for inserting target genes into plasmids. J. Biochem. Biophys. Methods *67*, 67–74. https://doi.org/10.1016/j.jbbm.2005.12.008.

84. Johnston, H.E., Yadav, K., Kirkpatrick, J.M., Biggs, G.S., Oxley, D., Kramer, H.B., and Samant, R.S. (2022). Solvent Precipitation SP3 (SP4) Enhances Recovery for Proteomics Sample Preparation without Magnetic Beads. Anal. Chem. *94*, 10320–10328. https://doi.org/10.1021/acs.analchem.1c04200.

85. Tsherniak, A., Vazquez, F., Montgomery, P.G., Weir, B.A., Kryukov, G., Cowley, G.S., Gill, S., Harrington, W.F., Pantel, S., Krill-Burger, J.M., et al. (2017). Defining a Cancer Dependency Map. Cell *170*, 564–576.e16. https://doi.org/10.1016/j.cell.2017.06.010.

86. Iorio, F., Knijnenburg, T.A., Vis, D.J., Bignell, G.R., Menden, M.P., Schubert, M., Aben, N., Gonçalves, E., Barthorpe, S., Lightfoot, H., et al. (2016). A Landscape of Pharmacogenomic Interactions in Cancer. Cell *166*, 740–754. https://doi.org/10.1016/j.cell.2016.06.017.

STAR★METHODS

KEY RESOURCES TABLE

REAGENT or RESOURCE	SOURCE	IDENTIFIER
Antibodies		
Rabbit anti-human MYC	Cell Signaling	5605; RRID:AB_1903938
Mouse anti-human MYCN	Merck	OP-13; RRID:AB_2266879
Rabbit anti-human NDUFAF4	Abclonal	A14345; RRID:AB_2761211
Rabbit anti-human vinculin	Abcam	ab129002; RRID:AB_11144129
Mouse anti-human α-tubulin	Merck	T5168; RRID:AB_477579
Goat anti-mouse secondary antibody, HRP conjugated	Advansta	R-05071-500; RRID: AB_10718209
Goat anti-rabbit secondary antibody, HRP conjugated	Advansta	R-05072-500; RRID: AB_10719218
IRDye® 680RD Goat anti-Mouse IgG Secondary Antibody	LI-COR	926-68070; RRID:AB_10956588
IRDye® 800CW Goat anti-Rabbit IgG Secondary Antibody	LI-COR	926-32211; RRID:AB_621843
Chemicals, peptides, and recombinant proteins		
IMP-1320	Myricx Bio	N/A
IMP-1088	Mousnier et al.[21]	N/A
DDD86481	Fang et al.[43]	N/A
Human recombinant NMT1	Goncalves et al.[72]	N/A
Human recombinant NMT2	Goncalves et al.[72]	N/A
CPM	Sigma-Aldrich	Cat#C1484
Src peptide (aa2-16)	Thinon et al.[9]	N/A
NDUFAF4 peptide (aa2-10, WT)	This paper, Francis Crick Institute	N/A
NDUFAF4 peptide (aa2-10, A3P)	This paper, Francis Crick Institute	N/A
Lipofectamine 2000	ThermoFisher Scientific	Cat#11668019
Phusion High Fidelity Polymerase	New England BioLabs	Cat#M0530
Sytox Green	ThermoFisher Scientific	Cat#S7020
Puromycin	Sigma-Aldrich	Cat#P8833
Triton X-114	Sigma-Aldrich	Cat#X-114
TCEP	Sigma-Aldrich	Cat#C4706
CAA	Sigma-Aldrich	Cat#C0267
Sequencing grade modified trypsin	Promega	Cat#5111
Poly-L-ornithine	Sigma-Aldrich	Cat#A-004-M
Oligomycin	Sigma-Aldrich	Cat#75351
FCCP	Sigma-Aldrich	Cat#C2920
Antimycin A	Sigma-Aldrich	Cat#A8674
Rotenone	Sigma-Aldrich	Cat#R8875
Hoechst 33342	ThermoFisher Scientific	Cat#H1399
MG132	Merck	Cat#M8699
YnMyr	Thinon et al.[9]	N/A
Azido-TAMRA-biotin	Broncel et al.[73]	N/A
Azido-TAMRA	Kallemeijn et al.[39]	N/A
TBTA	Sigma-Aldrich	Cat#678937
Lysing Matrix A	MP Biomedicals	Cat#1169100-CF
FxCycle Violet	ThermoFisher Scientific	Cat#F10347

(Continued on next page)

Continued

REAGENT or RESOURCE	SOURCE	IDENTIFIER
Zombie NIR	Biolegend	Cat#423105
CytoFix/Cytoperm	BD Bioscience	Cat#554714
Perm/Wash Buffer	BD Bioscience	Cat#554723
MitoTracker Red	ThermoFisher Scientific	Cat#M22425
MitoTracker Red CMXRos	ThermoFisher Scientific	Cat#M7512
4-OH-Tamoxifen	Sigma-Aldrich	Cat#H6278
β-estradiol	Sigma-Aldrich	Cat#E8875
Doxycycline hyclate	Sigma-Aldrich	Cat#D9891
Tetracycline-free FBS	ThermoFisher Scientific	Cat#A4736201
HEPES (1 M)	ThermoFisher Scientific	Cat#15630080
Sodium pyruvate (100 mM)	ThermoFisher Scientific	Cat#11360070
Penicillin-Streptomycin (10000U/mL)	Sigma-Aldrich	Cat#P4333
MEM non-essential amino acids (100x)	ThermoFisher Scientific	Cat#11140050
β-mercaptoethanol (50 mM)	ThermoFisher Scientific	Cat#31350010
Critical commercial assays		
CellTiter-Glo	Promega	Cat# G7572
DNeasy Blood & Tissue Kit	QIAGEN	Cat#69504
Mitochondria Isolation Kit for Cultured Cells	ThermoFisher Scientific	Cat#89874
TMT 10plex Isobaric Label Reagent	ThermoFisher Scientific	Cat#90111
CellTiter-Blue	Promega	Cat#G8090
Deposited data		
TX-114 fractionated proteomics data for SHEP21N cells	ProteomeXchange	PRIDE: PXD054008
TX-114 fractionated proteomics data for P493-6 cells	ProteomeXchange	PRIDE: PXD054019
Mitochondrial proteomics data for P493-6 cells	ProteomeXchange	PRIDE: PXD056941
In vivo DoHH2 proteomics data	ProteomeXchange	PRIDE: PXD063851
In vivo TH-*MYCN* proteomics data	ProteomeXchange	PRIDE: PXD063661
DepMap gene expression and essentiality (2023Q4 and 2024Q2)	Broad Institute	N/A
Sanger Project Score gene essentiality	Wellcome Sanger Institute	N/A
GDSC mutation and copy number alteration data	Wellcome Sanger Institute	N/A
SHEP21N ChIP-Seq data	Zeid et al.[74]	GEO: GSE80154
Experimental models: Cell lines		
Human embryonic kidney cell line HEK293	Francis Crick Institute	ATCC CRL-1573; RRID: CVCL_0045
Human cervical cancer cell line HeLa	Francis Crick Institute	ATCC CCL2; RRID: CVCL_0030
Human diffuse large B-cell lymphoma cancer cell line LY11212	EPO-GmbH	N/A
Human neuroblastoma cancer cell line MYCN-ER-SHEP	Hogarty Lab, Penn	N/A
Human neuroblastoma cancer cell line SHEP21N	Lin Lab, BCM	RRID:CVCL_9812
Human lymphoblastoid cell line P493-6	Dang Lab, LICR	DSMZ ACC 915; RRID:CVCL_6783
Mouse neuroblastoma cancer cells TH-*MYCN*	Institute for Cancer Research	N/A
Human non-Hodgkin's B-cell lymphoma cell line DoHH2	Crown Bioscience	RRID:CVCL_1179
Experimental models: Organisms/strains		
Mouse: 129SvJ	Institute for Cancer Research	RRID:IMSR_APB:4788
Mouse: CB17/SCID	Crown Bioscience	RRID:IMSR_RJ:CB17-SCID
Mouse: IL2R-NSG	Francis Crick Institute	RRID:IMSR_JAX:005557

Continued

REAGENT or RESOURCE	SOURCE	IDENTIFIER
Oligonucleotides		
Please see Table S2 for gRNA and primers used in this study.		N/A
Recombinant DNA		
gRNA_cloning vector	Church lab, Wyss Institute	Addgene plasmid 41824
pCas9_GFP	Musunuru Lab, Penn	Addgene plasmid 44719
Software and algorithms		
Prism 10	GraphPad	N/A
FinchTV	Geospiza, Inc.	N/A
ImageJ v1.54	Schneider et al.[75]	https://imagej.net/ij/download.html
ImageStudio	LI-COR	N/A
MaxQuant (v1.5.6.5 and v1.6.10.43)	Cox et al.[76]	https://maxquant.org/
DIA-NN v1.8.1	Demichev et al.[77]	https://github.com/vdemichev/DiaNN
Perseus (v1.5.6.0 and v1.6.14.0)	Cox et al.[78]	https://www.maxquant.net/perseus/
Cytoscape v3.10.1	Shannon et al.[79]	https://cytoscape.org/download.html
Metascape v3.5.20250101	Zhou et al.[80]	https://metascape.org
FlowJo	Tree star	N/A
Wave	Agilent Technologies	N/A
Other		
EnVision 2102 Multilabel Plate Reader	PerkinElmer	N/A
FACSAria III Cell Sorter	BD Biosciences	N/A
NanoDrop 2000c	ThermoFisher Scientific	N/A
IncuCyte S3	Sartorius	N/A
ImageQuant LAS4000	GE Healthcare	N/A
LI-COR Odyssey CLx	LI-COR	N/A
Savant SPD1010 SpeedVac® Concentrator	ThermoFisher Scientific	N/A
FastPrep 24	MP Biomedicals	N/A
Seahorse XFe96 extracellular flux analyzer	Agilent	N/A
Biacore S2000 Biosensors	Cytiva	N/A
Typhoon FLA 9500 imager	GE Healthcare	N/A
MACSQuant VYB	Miltenyi Biotec	N/A

EXPERIMENTAL MODEL AND STUDY PARTICIPANT DETAILS

Cell lines

The HEK293, SHEP21N, P493-6, DoHH2 and HeLa cells were authenticated by STR profiling by The Francis Crick Institute or Crown Bioscience. All cells were cultured in humidified 37°C incubators at 5% (v/v) CO_2 atmosphere. HEK293, MYCN-ER-SHEP and LY11212 cells were cultured in DMEM medium (with GlutaMAX) supplemented with 10% FBS, 10 mM HEPES, 1 mM sodium pyruvate, penicillin-streptomycin (100 U/ml and 100 μg/mL, respectively), 0.1 mM non-essential amino acids and 25 μM β-mercaptoethanol. HeLa cells were cultured in the same medium, except β-mercaptoethanol was not added. P493-6 cells were cultured in the same medium, except tetracycline-free FBS was used.

SHEP21N cells were cultured in RPMI-1640 medium supplemented with 10% tetracycline free FBS. The low MYC state in P493-6 cells was induced by addition of 0.1 μg/mL doxycycline and 1 μM β estradiol, and the low MYCN state in SHEP21N cells was induced by addition of 0.5 μg/mL doxycycline, for 24 h. The low MYCN state in MYCN-ER-SHEP cells was induced by addition of 200 nM 4-OH-Tamoxifen for 24 h.

LY11212 was derived from a female patient of unknown age diagnosed with DLBCL, classified as GCB using nanostring, CD20+, CD10+, BCL6+, IRF4neg, BCL2+, MYC+, Ki67 80% by histology and CD19+, IgM+, lambda+ by flow cytometry, with BCL2 translocation t(14; 18)(q32; q21) and MYC translocation t(8; 14)(q24; q32) by FISH.

All cell lines are of female origin, apart from the P493-6 line, which is unspecified. All cell lines were routinely tested for mycoplasma.

Mouse models

For the TH-*MYCN* syngeneic neuroblastoma model, 1×10^6 TH-*MYCN* tumor cells were injected subcutaneously into the right flank of 70–100 day old male and female 129SvJ mice and allowed to establish an syngeneic model. Mice bearing NB tumors with a mean diameter of about 5 mm were treated with IMP-1320 (25 mg/kg), or vehicle (PB buffer, pH 7.4) dosed via intraperitoneal injection QD, using a 3 days on, 4 days off cycle for 3 cycles. Tumor volumes were plotted until half the control mice reached the ethical endpoint. Studies were terminated when the mean diameter of the tumor reached 15 mm. Tumor volumes were measured by Vernier caliper across two perpendicular diameters, and volumes were calculated according to the formula $V = 4/3\pi [(d1+d2)/4]^3$; where d1 and d2 were the 2 perpendicular diameters.

Transgenic TH-*MYCN* mice were genotyped to detect the presence of human MYCN transgene.[64] Male or female mice with palpable tumors (30–50 days old) were treated with IMP-1320 (25 mg/kg) or vehicle (PB buffer, pH 7.4) dosed via intraperitoneal injection QD for 3 days and sacrificed 2 h after the final dose.

Mice were maintained on a regular diet in a pathogen-free facility on a 12-h light/dark cycle with unlimited access to food and water. All experiments were approved by The Institute of Cancer Research Animal Welfare and Ethical Review Body and performed in accordance with the UK Home Office Animals (Scientific Procedures) Act 1986 and the UK National Cancer Research Institute guidelines for the welfare of animals in cancer research.

For the DoHH2 model, experiments were carried out by the CRO Crown Bioscience. 5×10^6 cells/100 µL/body of DoHH2 resuspended in 50% PBS and 50% Matrigel were injected subcutaneously into the right flank of female six to seven week old CB17/SCID mice. Mice bearing DoHH2 xenografts with a mean tumor volume of around 120 mm^3 were treated with vehicle (10mM Na2HPO4 + 0.2% Tween-80) or IMP-1320 (25 mg/kg/day), dosed via intraperitoneal injection at 12.5 mg/kg BID, using a 3 days on, 3 days off cycle for 2 cycles (efficacy study) or for 3 days and sacrificed 2 h after the final dose (proteomic study). Tumor volumes were calculated as $0.5 \times$ length $\times$ width^2. CB17/SCID mice were maintained on a 12-h light/dark cycle with unlimited access to food and water. All experiments using CB17/SCID mice were conducted in accordance with an approved IACUC protocol and Crown Bioscience SOPs.

For the LY11212 model, six-to-seven-week old female NSG (IL2R-NSG) mice were provided from the Francis Crick Institute BRF facility. 1×10^7 cells/100 µL/body of LY11212 resuspended in 50% PBS and 50% Matrigel (Corning 356230) were transplanted subcutaneously into the right flank of each female. After three days, mice were treated with DDD86481 (25 mg/kg), or vehicle dosed via intraperitoneal injection once daily ($n = 10$ mice per group). Tumor volumes were calculated as $1/2 \times$ length $\times$ width^2. DDD86481 was resuspended in phosphate buffer containing 5% DMSO (Sigma D8418), 20% PEG400 (Hampton Research HR2-603) and 0.5% Tween-80 (Sigma P4780). Mice were housed in a specific-pathogen-free facility on a 12-h light/dark cycle with unlimited access to food and water. All experiments using IL2R NSG mice were carried out in accordance with national and institutional guidelines for animal care and were approved by The Francis Crick Institute biological resources facility strategic oversight committee (incorporating the Animal Welfare and Ethical Review Body) and by the Home Office, UK. All animal care and procedures followed guidelines of the UK Home Office according to the Animals (Scientific Procedures) Act 1986 and were approved by Biological Research Facility at the Francis Crick Institute.

METHOD DETAILS

Enzymatic NMT assays

Full-length human NMT1 and NMT2 were produced as described previously[72] and used at the final concentration of 300 ng/mL.[21] The assay buffer (pH 7.8) contained 5 mM phosphate buffer, 0.125 mM EDTA, 0.025% Triton X-100 and 1% DMSO. The assays were performed in 96-well black plates (110 µL total volume) using IMP-1088, IMP-1320 and DDD86481. Reactions were run for 30 min at room temperature and quenched with 60 µL 100 mM acetate buffer pH 4.8. NMT activity was determined through fluorescent detection of CoA-SH with 8 µM CPM (λex 380 nm, λem 470 nm, EnVision 2102 multilabel plate reader, PerkinElmer), formed during the *N*-myristoylation of 4 µM SRC peptide (amino acids 2–16), using 4 µM myristoyl-CoA.[9] After background correction, IC$_{50}$ values were determined by fitting the four-parametric variable slope function in Prism (GraphPad). Note that the lower limit for accurate determination of IC$_{50}$ values is 5 nM. For NDUFAF4 peptide (amino acids 2–10) assays the concentrations of WT and A3P peptides were varied. After background correction, Km values were determined by Michaelis-Menten function (nonlinear regression fit) in Prism. All assays were performed in at least two independent experiments.

Cell line panel

Screening was carried out using the OmniScreen platform (Crown BioScience, Beijing). Cells were plated into a 96 well plate and allowed to settle overnight. Cells were then treated with IMP-1320 (0–1 µM) for 72 h and viability measured using CellTiter Glo (Promega, G7572) according to manufacturer's instructions. IC$_{50}$ values were calculated using Prism (GraphPad).

Cell line screen analysis

Publicly available transcriptomic profiles for the 211 cell lines on Depmap were downloaded (RNAseq read count data from RSEM, Public 23Q4 release). The gene expression matrix was filtered to eliminate invariant and low expressed genes using the filterByExpr function in the edgeR package, using default parameters. The resulting gene expression matrix was normalised (TMM method) and

then converted in pathway expression indexes using ssGSEA on Hallmark gene sets from the Molecular Signature Database (MSigDB). Differentially expressed pathways between sensitive and less-sensitive cell lines were identified using a linear model with cancer type as a confounding variable. Pathways with an FDR<1% were considered significantly differentially expressed. Each statistically significant pathway was then assessed for its ability to discriminate between sensitive and less sensitive lines by calculating the Area Under the Curve (AUC) of a Receiver operating characteristic curve (ROC).

Cloning

gRNA_cloning vector was a gift from George Church (Addgene plasmid 41824),[60] and pCas9_GFP was a gift from Kiran Musunuru (Addgene plasmid 44719).[81] gRNA were designed using ChopChop tools[82] and synthetized according to the Church lab protocol.

Full-length human NDUFAF4 gene was ordered as a 525 bp geneblock from Integrated DNA Technologies. The NDUFAF4 gene was cloned into a C-FLAG pcDNA3 vector by restrictionless cloning using KOD polymerase for expression as a C-terminal FLAG-tagged construct.[83] To incorporate the G2A and A3P mutations, corresponding substitutions were introduced into forward primers used for restrictionless cloning. The inserts were confirmed by DNA sequencing. gRNAs and primers used for cloning and sequencing are listed in Table S2.

Generation of NMT1 and NMT2 CRISPR-Cas9 knockout clones in HeLa cells

$5x10^9$ HeLa cells/mL were seeded on 10 cm dishes. 24 h later, 2 μg of pCas9_GFP plasmid alone (control) or in parallel with 2 μg of the respective gRNA (Table S2) was transfected using Lipofectamine 2000 (ThermoFisher Scientific 11668019) according to the manufacturer's instructions. 48 h later, cells were harvested and sorted by BD FACSAria III according to the GFP fluorescence at Imperial College South Kensington facility, in 96 flat-bottom well plates to generate single cell clones. Clones where lack of NMT1 and NMT2 protein was verified by western blot, were sequenced to confirm successful knockouts.

Verification of CRISPR-Cas9 knockouts by sequencing

Genomic DNA (gDNA) was extracted from every clone using DNA extraction kit (QIAGEN 69504) according to the manufacturer's instructions. gDNA concentration was measured using a NanoDrop 2000c spectrophotometer (ThermoFischer Scientific). Because the final PCR product was used for sequencing analysis, PCR amplification reactions were performed using Phusion High Fidelity Polymerase (New England BioLabs M0530). Primer sequences are indicated in Table S2. PCR was performed in a final volume of 25 μL, containing 10 μL of 2x PCR Master Mix, 1.25 μL of forward primers, 1.25 μL of reverse primers, 40 ng of gDNA, and water. PCR amplifications were performed according to the following parameters: 98°C for 30 s; 25–35 cycles (suitable cycles were chosen for each gene) of 98°C for 5–10 s, 56°C–65°C (proper annealing temperature was chosen for gene) for 10 s, and 72°C for 15–30 s, with a final extension step of 72°C for 5 min. The PCR product was then purified and sent for sequencing to Genewiz (Sanger Sequencing). Chromatograms were analyzed using FinchTV.

NMTi treatment

P493-6 and SHEP21N were seeded in 6-well plates, allowed to attach overnight, and MYC and MYCN states induced as described above. Cells were then treated with DMSO or 100 nM IMP-1088 for 18 h.

Cells were lysed using PBS with 1% Triton X-100, 0.1% SDS and 1x cOmplete EDTA-free protease inhibitor cocktail (Roche, 11873580001), insoluble material removed by centrifugation (17,000g, 10 min, 4°C) and protein concentration determined using the DC Protein Assay Kit II (Bio-Rad, 5000112).

Real-time cytotoxicity assay

Cells were first induced into the relevant MYC (P493-6) or MYCN (SHEP21N) state for 24 h, then seeded into 96 well plates (P493-6, $1x10^4$ cells; SHEP21N, $2x10^3$ cells). The next day, 250 nM Sytox Green (ThermoFisher Scientific, S7020) and DMSO or IMP-1088 were added to cells in technical triplicate. 2 μg/mL puromycin (Sigma, P8833) was used as a positive control. Cells were monitored using the IncuCyte S3 platform (Sartorius). Image acquisition was performed every 4 h for 120 h using the phase and green channels and analyzed using the Incucyte software. Cell death was defined as green area over phase area. Values were normalized by dividing by the puromycin AUC. Experiments were repeated for three independent replicates.

Western Blot

Protein samples were prepared with 4x Laemmli sample loading buffer (BioRad 1610747) and 10% β-mercaptoethanol, boiled for 5 min at 95°C and resolved on 10% or 12% (w/v) SDS-PAGE gels running at 180 V.

For MYCN induction and NDUFAF4 expression experiments in SHEP21N cells, proteins were transferred onto nitrocellulose membrane for 1 h using wet blotting and blocked for 1 h with 5% (w/v) skimmed milk in TBS 0.1% Tween 20. Proteins were detected using MYC (Cell Signaling, 5605), MYCN (Merck, OP-13), NDUFAF4 (ABclonal, A14345), and vinculin (abcam, ab129002). HRP-conjugated secondary antibodies (Advansta, R-05071-500 and R-05072-500) were used to detect proteins by ImageQuant LAS4000 (GE Healthcare), quantified by ImageJ[75] (NIH Bethesda), and normalized against the loading control.

For NDUFAF4 experiments in P493-6 and HEK293 cells, proteins were transferred onto nitrocellulose membrane using Trans-Blot Turbo (BioRad) and blocked for 30 min with 5% (w/v) BSA in TBS 0.2% Tween 20. Proteins were detected using NDUFAF4 (ABclonal,

A14345), α-tubulin (Sigma, T5168). Fluorescence signal from secondary antibodies (LI-COR) was quantified using the Odyssey LI-COR system. Quantification was performed using Image Studio software (LI-COR) and statistical analysis was performed using Prism (GraphPad). Uncropped Western blots are shown in Figures S8 and S9.

TX-114 fractionated proteomics

P493-6 cells were seeded in in a T175 at 5×10^5 cells/ml in 30 mL and incubated overnight. Cells were then treated with 100 nM IMP-1088 or DMSO control for 24 h, with each condition performed in biological quadruplicate. 1×10^7 SHEP21N cells were seeded in a T175 and allowed to attach overnight. The following day, cells were treated with 50 nM IMP-1088 or DMSO control for 18 h, with each condition performed in biological triplicate. Cells were then harvested, centrifuged, washed twice with PBS and the cell pellet stored at $-80°C$ until lysis.

Cell pellets were resuspended in PBS containing 2% (w/v) condensed TX 114 (Sigma, X-114) and 1x cOmplete EDTA free protease inhibitor cocktail, lysed by shaking (800 rpm, 30 min, 4°C), and debris removed by centrifugation at 17,000g for 10 min at 4°C.

Phase separation was induced as previously described.[45] In brief, the supernatant was incubated at 37°C for 10 min, followed by centrifugation (17,000g, 10 min, rt). The detergent (bottom) phase was kept, washed with 0.1% TX114 (w/v) in PBS and the mixture clarified on ice. This was repeated three times, and the bottom phase kept as the detergent-enriched membrane fraction. Proteins were precipitated by chloroform methanol, washed twice with methanol, and resuspended in 0.2% SDS (w/v) in 50 mM HEPES pH 8.0. Protein concentrations were determined, adjusted to 1 mg/mL and 50 μg protein per condition taken forward.

Proteins were reduced and alkylated with 10 mM TCEP and 40 mM CAA for 5 min at 70°C, precipitated by SP4,[84] and resuspended in 25 mM ammonium bicarbonate. Samples were then digested with 0.8 μg trypsin (Promega, V5111) at 37°C overnight. Solvent was removed using a Savant SPD1010 SpeedVac Concentrator (ThermoFisher Scientific) at 45°C and peptides were then rehydrated in LC MS grade H2O containing 2% (v/v) acetonitrile and 0.5% (v/v) TFA ready for injection into the LC MS/MS. Peptides were analyzed on an Orbitrap Eclipse mass spectrometer coupled to an Ultimate 3000 RSLCnano HPLC (ThermoFisher Scientific) using an Easy Spray Nano-source or a timsTOF HT (Bruker) coupled to an Evosep One (Evosep).

Data-dependent acquisition

Peptides (3 μL, 0.25 μg/μL) were loaded on to a trap column (Acclaim PepMap 100 75 μm × 2cm nanoViper; ThermoFisher Scienific) using loading buffer (2% MeCN, 0.05% TFA). Peptides were separated using an PepMap RSLC C18 50cm column (ThermoFisher, ES803) using an EasySpray source using a gradient of 2–40% buffer B over 93 min a flow rate of 275 nL/min. The column was held at 40°C. Analytical solvents A: 5% DMSO, 0.1% FA and B: 75% MeCN, 5% DMSO and 0.1% FA. Survey scans were acquired by the Orbitrap Eclipse at a resolution of 120,000 at m/z 200. Scans were acquired from 350 to 1500 m/z with the following parameters: RF Lens 30%, AGC Target 400,000, and maximum injection time 50 ms. Monoisotopic Precursor Selection (MIPS) was set to peptide. Dynamic exclusion was enabled with an exclusion duration of 20 s after 1 times, with a mass tolerance of ±10 ppm. The minimum intensity was set to 10,000. Precursors with charge states 2–6 were selected for MS/MS with an isolation window of 1.2 m/z, AGC Target of 10,000 and a maximum injection time of 100 ms. Precursor ions were fragmented by HCD with a collision energy of 30%. MS2 Scans were obtained in the ion trap at a rapid scan rate and obtained in centroid mode.

Data-independent acquisition

Peptides (200 ng) were loaded onto EvoTips (Evosep) as per manufacturer's instructions and separated by the Evosep 60SPD work-flow using an 8cm, 150μm, 1.5μm analytical column (Evosep). Analytical solvents A: 0.1% FA and B: MeCN and 0.1% FA. Column was held at 40°C. Data were acquired in data-independent acquisition PASEF mode with the following settings: m/z range from 100 m/z to 1700 m/z, ion mobility range from $1/K0 = 1.30$ to 0.85 Vs/cm^2 using equal ion accumulation and ramp times in the dual TIMS analyser of 100 ms each. Each cycle consisted of 8 PASEF ramps covering 21 mass steps each with 25 Da windows each with 2/3 non-overlapping ion mobility windows covering the 475 to 1000 m/z range and 0.85 and 1.26 Vs/cm^2 ion mobility range. The collision energy was lowered as a function of increasing ion mobility from 59 eV at $1/K0 = 1.6$ Vs/cm^2 to 20 eV at $1/K0 = 0.6$ Vs/cm^2.

Proteomics data analysis

Data obtained from the Eclipse were processed using MaxQuant[76] (version 1.6.10.43), using the inbuilt Andromeda search engine.[78] The MS/MS spectra were matched against the human reference proteome with isoforms (UniProt, accessed January 2022). Cysteine carbamidomethylation was defined as a fixed modification; methionine oxidation, N terminal acylation and N terminal *N*-myristoylation were set as variable modifications. As digestion mode 'Trypsin/P' was chosen, and a maximum of two missed cleavages allowed. Both the options 'match between runs' and 'unique and razor peptides' for protein quantifications were selected. Data were quantified using LFQ with a minimum ratio count of 2.

diaPASEF Bruker.d files were processed using library-free analysis in DIA-NN[77] (version 1.8.1) using the following parameters: Human database (UniProt, accessed 13 July 2023 and containing 246 common contaminants); "deep learning-based spectra and RTs prediction" was enabled; trypsin with 1 missed cleavages; N-term Excision, C carbamidomethylation, Oxidation and N terminal Acetylation were enabled with maximum 2 variable modifications; MBR was enabled; quantification strategy set to "Robust LC (high precision)"; heuristic protein inference was disabled; Mass and MS1 accuracy set to 0.

The processed data was then further analyzed with Perseus (version 1.6.14.0) using MaxQuant proteingroups.txt and DiaNN report.pg_matrix.tsv. Maxquant protein groups were filtered against contaminants, reverse and proteins identified by site; DiaNN protein groups were filtered against contaminants. LFQ intensities were transformed using a base 2 logarithm. For each experiment, datasets were filtered to allow one missing value in each experimental condition (DMSO or IMP-1088 treated). For every protein, a two-tailed unpaired Student's t-test was performed with FDR = 0.05 and proteins with a p value <0.05 were considered significant.

Protein interaction networks were generated using stringApp (v2.0.1) in Cytoscape[79] (version 3.10.1) considering a high confidence interactors (confidence cut off 0.7) and the physical subnetwork only.

Oxygen consumption rate measurements

Oxygen consumption rate was measured using Seahorse XFe96 extracellular flux analyzer (Agilent Technologies) according to the manufacturer's protocols. Seahorse cartridge (Agilent Technologies) was hydrated in 200 μL XF calibrant solution (Agilent Technologies) overnight in a non-CO_2 incubator at 37°C. For the suspension cells, 5×10^5 cells/ml of P493-6 cells were grown as described before in a 6-well plate in the different MYC conditions (low- and high-MYC) for 24 h, and 5×10^5 cells/ml of LY11212 cells were grown as described before. NMT inhibitors (100 nM IMP-1088 or 1 μM DDD86481) were added for an additional 18 h. On the day of the assay, the 96-well Seahorse cell culture plate (Agilent Technologies) was coated with 0.01% poly-L-ornithine solution (Sigma, A-004-M) for 2 h prior to seeding 5×10^4 cells/well (P493-6) or 1×10^5 cells/well (LY11212) in 50 μL of Seahorse XF base medium (unbuffered DMEM with phenol red), containing 10 mM glucose, 1 mM sodium pyruvate and 2 mM L-glutamine. To allow the cells to adhere to the bottom, the plate was centrifuged at 200g for 1 min with the lowest break setting. The seeded plate was placed into a non-CO_2 incubator at 37°C for 20 min after which an additional 130 μL of the culture medium was added to the wells. The plate was then placed into a non-CO_2 incubator at 37°C for 20 min before running the assay. The cartridge injection ports A, B and C were filled with 20 μL of oligomycin (15 μM), 22 μL of carbonyl cyanide-4 (trifluoromethoxy) phenylhydrazone (FCCP) (20 μM) and 25 μL of rotenone/antimycin A mixture (5 μM each) diluted in Seahorse XF base culture medium to give the final assay concentrations of 1.5 μM oligomycin, 2 μM FCCP and 0.5 μM rotenone/antimycin A (injected in the same order). Oligomycin, FCCP, antimycin A and rotenone were purchased from Sigma Aldrich or Agilent. Mixing, waiting and measurement time were set to 2, 2 and 4 min respectively. For the adherent SHEP21N line, 3×10^5 cells/well were seeded in a 96-well Seahorse cell culture plate, allowed to attach for 8 h, then treated with 100 nM IMP-1088 for 18 h. On the day of the assay, the media in the 96-well Seahorse cell culture plate was exchanged to 180 μL of Seahorse XF RPMI medium (unbuffered RPMI without phenol red) containing 10 mM glucose and 2 mM L-glutamine and the plate placed into a non-CO_2 incubator at 37°C for 50 min before running the assay. The default mixing, waiting and measurement times were used. Cartridge injection ports were filled as for the suspension cells except 22 μL of FCCP (5 μM) was used for port B to give a final assay concentration of 0.5 μM FCCP and Hoechst (25 mM, 1:1000 dilution) was added to the rotenone/antimycin A mixture to allow for normalisation by DNA staining after assay completion (CLARIOstar *Plus*, BMG LABTECH). The data were obtained using Wave software (Agilent Technologies) and analyzed with Prism (GraphPad).

Mitochondrial proteomics

P493-6 cells were cultured for 18 h in the respective MYC conditions at 1×10^6 cells/ml in 10 mL in 10-cm diameter dishes. The high-MYC and low-MYC cells were subsequently treated with 100 nM IMP-1088 or DMSO for 18 h, with each condition performed in biological triplicate. Cells were harvested, centrifuged and washed with PBS. Cell pellets were then processed using the Mitochondria Isolation Kit for Cultured Cells (ThermoFisher Scientific, 89874) following the manufacturer's instructions. The mitochondrial pellets were homogenized by sonication in lysis buffer containing 1% (v/v) Triton X-100, 0.1% (w/v) SDS and EDTA-free protease inhibitor cocktail in PBS, pH 7.4. Protein concentrations were determined and lysate (50 μg) was precipitated by chloroform-methanol, washed with MeOH, and resuspended in 50 μL HEPES, pH 8.0. Proteins were reduced and alkylated using 5 mM TCEP and 15 mM CAA for 45 min at rt with vortexing, and subsequently digested by trypsin for 18 h at 37°C and shaking at 1,100 rpm. Peptides were then labeled with TMT10plex Isobaric Label Reagent (ThermoFisher Scientific, 90111), fractionated and analyzed by nanoLC-MS/MS on a Thermo Q-Exactive instrument as described previously.[20,21]

Mitochondrial proteomics analysis

The data were processed using MaxQuant (version 1.5.6.5) using the built-in Andromeda search engine. The MS/MS spectra were matched against the human reference proteome with isoforms (UniProt, accessed December 2020). TMT10plex was set per sample group, and the reporter ion MS2 correction factors were included as supplied by the manufacturer. Cysteine carbamidomethylation, methionine oxidation and N-terminal acylation were set as variable modifications. As digestion mode 'Trypsin/P' was chosen, and a maximum of two missed cleavages allowed. Both the options 'match between runs' and 'unique and razor peptides' for protein quantifications were selected. The processed data was then further analyzed with Perseus (version 1.5.6.0). Protein groups were filtered against contaminants, reverse and proteins identified by site, and TMT intensities transformed using a base 2 logarithm. Proteins involved in mitochondrial respiratory complex 1 (mtRC1, with proteins reported in 59) annotated in the plots. The $\log_2$ fold changes observed for the mtRC1 proteins identified were plotted, Tukey box-plots were generated and the significance was calculated using Student t-test (two-tailed, heteroscedastic). Differences between responses of individual mtRC1 proteins in high- and low MYC to IMP-1088 were calculated by subtracting the $\log_2$ fold changes, then ranked and color-graded by difference.

NDUFAF4 biochemistry

HEK293 cells were plated in 6-well plates and transfected with NDUFAF4-FLAG constructs (WT, G2A and A3P) using 2 μg of DNA plasmid and 6 μL of Fugene HD transfection reagent (1:3 ratio) per well. 24 h after transfection, cells were treated with 10 μM of MG132 (Merck, M8699) or DMSO as a vehicle control for a further 16 h. Cells were lysed (lysis buffer: PBS with 1% Triton X-100, 0.1% SDS and 1x Complete EDTA-free protease inhibitor cocktail) and subjected to western blotting.

In vivo proteomics

Tumors were lysed by bead beating using Lysing Matrix A (MP Biochemicals, 1169100-CF) in 150 mM NaCl, 10 mM $CaCl_2$, 50 mM Tris pH 7.5 supplemented with cOmplete protease inhibitor and debris removed by centrifugation (17,000g, 10 min, 4°C). Samples were normalized to 2 μg/μL and 20 μg protein taken forward for proteomics. Proteins were reduced and alkylated with 10 mM TCEP and 40 mM CAA for 10 min at rt, precipitated by SP4, and resuspended in 25 mM ammonium bicarbonate containing 14 ng/μL trypsin. Samples were digested at 37°C overnight, and peptides acidified and diluted to 10 ng/μL using 0.1% formic acid (pH < 3). Peptides were analyzed using a timsTOF HT coupled to an Evosep One using the data-independent settings described above, except 250 ng of peptides were loaded and peptides were separated using the Evosep 30SPD workflow. Data were analyzed as described previously.[39]

Meta-analysis

Meta-analysis of DoHH2 and TH-*MYCN* proteomics was performed using Metascape v3.5.20250101.[80] Proteins significantly down-regulated by IMP-1320 treatment were submitted for Metascape analysis. Significance was set as $p < 0.05$. Proteins were analyzed as the relevant species against the CORUM[65] database only.

SPR

Kinetics data were collected on Biacore S200 Biosensors (Cytiva). Recombinant human NMT1 109-496aa proteins were immobilized to Series S CM5 sensorchips, which were maintained with a continuous flow of HBS-P+ (10 mM 4-(2-hydroxyethyl)-1-piperazineethanesulfonic acid adjusted to pH 7.4, 150 mM NaCl and 0.5% (v/v) polysorbate 20). 7 min, 10 μL/min injections of 0.5 M 1-ethyl-3-(3-(dimethylamino)propyl)-carbodiimide (EDC) and 0.1 M N-hydroxysuccinimide (NHS) facilitated catalytic activation of the carboxylate moieties of the surface dextran matrix. Recombinant NMT1 was exchanged into 10 mM Sodium Acetate pH5 buffer, at a final concentration of 10 μg/mL. Proteins were injected across the activated dextran surface for 50 s at 10 μL/min to achieve a low-density immobilization (500–1000 RU). Unreacted succinimide esters were deactivated with a 7 min injection of 1 M ethanolamine at 10 μL/min. For each protein-coupled flow cell, a reference flow cell was also prepared. Compounds were stored at 50 mM in 100% DMSO at 25°C. Stocks were diluted to 100 μM in DMSO, before being diluted to 1μM + 1% DMSO in HBS-P+. Compounds were diluted further to 10 nM, followed by a 5-point, 2-fold serial dilution (10 nM, 5 nM, 2.5 nM, 1.25 nM 0.625 nM) in HBS-P+ + 4 μM myristoyl-coenzyme A + 1% DMSO ("Assay Buffer"). Solvent correction samples were made in HBS-P+ with 4 μM myristoyl-coenzyme A with an 8-point increasing concentration of DMSO from 0.05% to 1.5%. The diluted compound series was injected in order of ascending concentration for 400 s, across a specific flow cell, separated by a 50 s flow of assay buffer. Dissociation was monitored during a 1500 s injection of assay buffer. An equivalent series of injections was carried out using Assay Buffer, which was used to correct flow cell-specific artifacts.

Public datasets

Gene expression data was obtained from the Broad DepMap project[85] (https://depmap.org/portal); Release 2023Q4 and normalised by the TMM method. The CRISPR data for gene essentiality was obtained from the Broad DepMap project[31,85]; Release 2024Q2 and from the Sanger Project Score project.[32] The pre-processed microarray data, coding variants and copy number alterations for analysis of data from the Sanger institute were obtained from the GDSC project.[86] SHEP21N ChIP-Seq data was downloaded from GSE80154.[74]

YnMyr labeling for in-gel fluorescence and streptavidin pulldown

P493-6 and LY11212 cells were treated with 100 nM IMP-1088, 1 μM DDD86481 or DMSO (negative control) for 30 min, followed by YnMyr (20 μM) and incubated for 18 h. SHEP21N cells were treated with 100 nM IMP-1088 or DMSO for 30 min, followed by YnMyr (20 μM) and incubated for 18 h. HEK293 cells were treated with YnMyr (20 μM) for 18 h. Lysates (PBS with 1% Triton X-100, 0.1% SDS and 1x Complete EDTA-free protease inhibitor cocktail) were subjected to ligation with 0.1 mM Azido-TAMRA-Biotin[73] (AzTB) or 0.1 mM Azido-TAMRA (AzT) in a click reaction buffer containing 1 mM $CuSO_4$, 1 mM TCEP and 0.1 mM TBTA for 1 h and analyzed by in-gel fluorescence using the Typhoon FLA 9500 imager (GE Healthcare). For streptavidin pulldown, cell lysate protein was chloroform-methanol precipitated, resuspended in 0.1% SDS and 5 mM DTT and Streptavidin MyOne beads (ThermoFisher Scientific) were added for 2 h (1000 RPM shaking at rt). Consistent gel loading was confirmed by Coomassie stain (Instant Blue, Expedeon) or by western blot using tubulin as a loading control, scanned using Odyssey CLx imager (LI-COR) and analyzed by ImageStudio software (LI-COR).

Cell viability measurements

CellTiter-Blue (Promega G8080) was employed to assess cell viability following exposure of the cells to different concentration of the respective NMT inhibitors. The experiments were carried out in 96-well flat bottom plates with three or four technical replicates. LY11212 cells were seeded at 5×10^5 cells/ml with 100 μL of culture medium containing the range of inhibitor concentrations or DMSO control. HeLa cells were seeded in 50 μL at 1.7×10^3 and 2×10^3 cells/well respectively in quadruplicate on 96 wells flat bottom. The following day, 50 μL with twice the concentration of IMP-1088 were added to the cells and 72 h later CellTiter-Blue was added following the manufacturer's instructions. Once the experiment reached the endpoint, 10 or 20 μL of CellTiter-Blue was added to each well and the plates were left at 37°C in the incubator for 2 h prior to measuring fluorescence at excitation/emission λ_{ex} 560 nm, λ_{em} 590 nm using the EnVision 2102 multilabel plate reader (PerkinElmer). Cell viability was normalized against the positive control (mixture of staurosporin and puromycin at the final concentration of 1 μg/mL and 10 μg/mL respectively). Prism (GraphPad) was used to fit the four-parametric variable slope function. Every experiment was repeated three times.

Flow cytometry

P493-6 cells were cultured for 24 h in the respective MYC conditions at concentration of 5×10^5 cells/ml. The following day, 50 μL of single cell suspension cells was added to 50 μL of culture medium containing twice the concentration of inhibitors or control and the respective MYC conditions in 96 U-well plates. For time course beyond 24 h, 100 μL of culture medium containing the respective MYC conditions, inhibitors, and control, were added to the cells. SHEP-ER-MYCN were seeded at 7×10^3 cells/mL in 24 well plates flat bottom. 24 h later, culture media containing 200 nM 4-OH-Tamoxifen or EtOH as control were added to the wells for 24 h. Culture medium was removed, and fresh medium containing 100 nM 4-OH-Tamoxifen, NMTi and DMSO controls were added to the respective wells for the time course indicated. DNA content was stained with FxCycle Violet (ThermoFisher Scientific, F10347) To exclude dead cells, Zombie NIR (423105, Biolegend) was used according to the manufacturer instructions. The cells were fixed with 4% PFA, and permeabilized employing CytoFix/Cytoperm (BD Bioscience 554714) and washed in perm/Wash Buffer (BD Bioscience, 554723). MACSQuant VYB (Miltenyi Biotech) was used to acquire the samples and analyzed using FlowJo software. Examples of gating strategies are provided in Figure S10.

Cytofluorimetry for MitoTracker staining

MitoTracker red (M22425) was used according to the manufacturer's instructions. Briefly, P493-6 were cultured overnight in the different MYC conditions as described previously. The following day, cells were transferred to a 96 U-well plates and treated for 18 h with 100 nM IMP-1088. Next, the plate was centrifuged, the culture medium was carefully removed, and the pellet was resuspended in a culture medium containing 200 nM of MitoTracker staining for 30 min at 37°C. The cells were then washed with PBS containing Zombie NIR for 5 min to discriminate the ones with intact membrane, re-pelleted and resuspended into prewarmed FACS buffer (PBS with 2% w/v FCS) and analyzed using MACSQuant VYB analyzers (Miltenyi Biotec). To analyze superoxide production, MitoTracker Red CMXRos (M7512) was used at the final concentration of 5 μM for 15 min. Cells were then treated as described for M22425 and run using MACSQuant. FlowJo software was used to analyze the data and the experiments were run in biological triplicate and every time in technical replicate.

QUANTIFICATION AND STATISTICAL ANALYSIS

Statistical analyses were carried out in Prism (GraphPad) and statistical significance defined as $p < 0.05$, except when specified otherwise. Significance for cell line panel IC_{50} results according to tissue type was determined by a student's t-test (two-tailed). Differentially expressed pathways between sensitive and less sensitive cell lines in the cell line screen were identified using linear model with cancer type as a confounding variable in R. Pathways with an FDR<1% were considered differentially expressed. Quantification of NDUFAF4 western blots were determined using densitometry of the NDUFAF4 and loading control bands and statistical significance determined by one-way ANOVA. Volcano plots for TX-114 fractionated proteomics datasets were constructed in Perseus using a two-tailed Student's t-test, with FDR set as 0.05 and S0 as 0.1. Significance for Seahorse parameters were determined by two-way or one-way (LY11212 experiments) ANOVA; for cell viability measured by CellTiter Blue by one-way ANOVA and for MitoTracker staining results by two-way ANOVA. Significance for the mtRC1 protein fold changes in P493-6 cells was determined by Student's t-test (two-tailed, heteroscedastic). Significance for *in vivo* tumor and body weight data was determined by two-way ANOVA or mixed-effects analysis and for *in vivo* effects on mtRC1 by the non-parametric, paired Wilcoxon t test.